

On the choice and implications of rheologies that maintain kinematic and dynamic consistency over the entire earthquake cycle

Rishav Mallick^{1,2}, Valère Lambert³, and Brendan Meade⁴

¹Seismological Laboratory, California Institute of Technology

²Earth Observatory of Singapore, Nanyang Technological University, Singapore

³Seismological Laboratory, University of California, Santa Cruz

⁴Department of Earth and Planetary Sciences, Harvard University

September 15, 2022

Abstract

Viscoelastic processes in the upper mantle redistribute seismically generated stresses and modulate crustal deformation throughout the earthquake cycle. Geodetic observations of these motions at the surface of the crust-mantle system offer the possibility of constraining the rheology of the upper mantle. Parsimonious representations of viscoelastically modulated deformation through the aseismic phase of the earthquake cycle should simultaneously explain geodetic observations of (1) rapid postseismic deformation, (2) late in the earthquake cycle near-fault strain localization. To understand how rheological formulations affect kinematics, we compare predictions from time-dependent forward models of deformation over the entire earthquake cycle for an idealized vertical strike-slip fault in a homogeneous elastic crust underlain by a homogeneous viscoelastic upper-mantle. We explore three different rheologies as inferred from laboratory experiments: (1) linear Maxwell, (2) linear Burgers, (3) power-law. The linear Burgers and power-law rheologies are consistent with fast and slow deformation phenomenology over the entire earthquake cycle, while the single-layer linear Maxwell model is not. The kinematic similarity of linear Burgers and power-law models suggests that geodetic observations alone may be insufficient to distinguish between them, but indicate that one may serve as an effective proxy for the other. However, the power-law rheology model displays a postseismic response that is strongly earthquake-magnitude dependent, which may offer a partial explanation for observations of limited postseismic deformation near some magnitude 6.5-7.0 earthquakes. We discuss the role of mechanical coupling between frictional slip and viscous creep in controlling the time-dependence of regional stress transfer following large earthquakes and how this may affect the seismic hazard and risk to communities living close to fault networks.

Main Language Summary

The solid Earth is a viscoelastic material that displays both solid and fluid-like behaviors depending on the observational time window and the applied stress. We develop numerical simula-

This article has been accepted for publication and undergone full peer review but has not been through the copyediting, typesetting, pagination and proofreading process, which may lead to differences between this version and the Version of Record. Please cite this article as doi: 10.1029/2022JB024683.

This article is protected by copyright. All rights reserved.

tions of how the uppermost solid Earth responds to a sequence of periodic earthquakes and the earthquake cycle. Our simulations test a range of proposed viscoelastic materials. The predicted surface displacements from each model are compared with observational features extracted from geodetic datasets compiled over the past few decades. All existing viscoelastic material descriptions can satisfactorily explain observational features in the first few years following an earthquake; significant differences between the viscoelastic models emerge 10 - 100 years following a large earthquake. Identifying the most appropriate viscoelastic description requires the integration of geodetic data that constrains the velocity evolution from a sequence of earthquakes (as opposed to a single event) with observations from rock physics laboratory experiments. A unified description of viscoelasticity in the uppermost solid earth has important implications for understanding stress evolution in fault networks, and improving models of seismic hazard.

1 Introduction

Inferring the constitutive relations that describe how the macroscopic stress state of the lithosphere-asthenosphere system evolves as a function of strain rate, total strain and intensive system variables (temperature, pressure, composition, etc.) remains a grand challenge in the geosciences [NSF, 2020]. Constraining these constitutive relations, or rheology, is fundamental to our understanding of the dynamics of the solid Earth. From the occurrence of earthquakes and their effects at any point within the Earth, to the construction of the geological structure that surrounds us and the sustenance of plate tectonics itself, the rheology and strength of Earth materials plays a crucial role in defining these processes [Bürgmann and Dresen, 2008; Mulyukova and Bercovici, 2019]. However, inferring these constitutive relations at the kilometer scale of geological processes is a difficult task as aspects of rock failure are shown to be scale-dependent [e.g., Yamashita *et al.*, 2015; Lambert *et al.*, 2021] and there are limited opportunities to conduct experiments at the crustal or lithospheric scale. Our goal in this article is to demonstrate that the earthquake cycle, in the vicinity of a mature strike-slip fault, may provide us with the necessary experimental conditions to probe the rheology of the lithosphere.

While there exist a number of studies that have sought to infer rheological properties of Earth's lithosphere-asthenosphere system using observations from the earthquake cycle [Bürgmann and Dresen, 2008, and references therein], the interpretation of results from different methodologies for extracting rheological parameters can be limited or challenged by three key assumptions. First, a common approach to modeling geophysical systems is to prescribe a functional form of the rheological model *a priori* and then estimate the associated best-fitting set of rheological parameters for that selected model, potentially with limited consideration of alternative rheological models that may be equally or better supported by the observations. Second, studies are often limited to a specific observational time window, such as a few years following an earthquake, from which the aforementioned best-fit model parameters are estimated. As such, inferred parameters are tied to the observational window that is probed, which may in part explain vastly different rheological estimates determined for studies of the lithosphere over different observational windows [e.g., Pollitz, 2005, 2019; Ryder *et al.*, 2007; Henriet *et al.*, 2019; Tamisiea *et al.*, 2007; Milne *et al.*, 2001; Hussain *et al.*, 2018; Larsen *et al.*, 2005; Kaufmann and Amelung, 2000]. Finally, a common assumption when processing observed time series is that the signal can be well-separated into a set of linearly superimposed functions, thereby neglecting nonlinear interactions among the associated physical processes.

In this work, we seek to develop a framework that overcomes some of these limitations and can reconcile rheological inferences from different observational windows. As a starting point,

we focus on major observational features in geodetic time series obtained from mature strike-slip fault settings globally, from immediately following earthquakes (postseismic period) to late in the earthquake cycle (interseismic period). We do not attempt to directly optimize the fit to data, rather we consider the generality and descriptive power of popular rheological models of the lithosphere and study where each model can explain major observational features or is insufficient [Tarantola, 2006]. To assist the reader with appreciating the task at hand, we begin by providing some background on common rheological models that are used to describe lithospheric deformation, general observational constraints available from geodesy and prevalent modeling strategies in the literature.

1.1 Elasticity, friction and viscous creep

The rheology of the lithosphere does not appear to follow a single simple description at all timescales. For example, observations of the passage of seismic waves and the static deformation of the Earth's lithosphere, in response to an earthquake, allow us to describe the lithosphere as an elastic body over timescales ranging from seconds to a day. However, the entire lithosphere cannot be elastic since an earthquake source is a frictional rupture restricted to a narrow shear band [Kanamori and Brodsky, 2004]. At timescales longer than a day, time-dependent deformation patterns of the solid Earth's surface following large earthquakes reveal the non-elastic nature of the lithosphere i.e., deformation that continues well after the initial source of deformation has ceased, and is thought to result from a combination of two different processes: (1) time-dependent frictional slip on fault planes (afterslip) while the surrounding medium is elastic [Marone *et al.*, 1991], and (2) time-dependent distributed deformation of the entire medium itself. This is commonly modeled as a viscoelastic process where the short timescale stress perturbations are accommodated by the elasticity of the medium ($\varepsilon \propto \sigma$), while relaxation following instantaneous stress steps or long timescale observations highlight the viscous properties of the medium i.e., $\dot{\varepsilon} \propto \sigma^n$ (ε - strain, $\dot{\varepsilon}$ - strain rate, n - power exponent, σ - stress) [Hirth and Kohlstedt, 2003]. Laboratory experiments also suggest that viscous flow laws exhibit unsteady or transient deformation i.e., the relationship between σ and $\dot{\varepsilon}$ is unique once steady state is achieved, which requires a finite amount of strain or time [Post, 1977]. This style of deformation is often modeled using a Burgers rheology [e.g., Müller, 1986; Hetland and Hager, 2005].

1.2 Geodetic observations

In this study, we focus on mature strike-slip faults and simplify them to a two-dimensional geometry and describe the characteristics of the interseismic and postseismic period as imaged by the past few decades of geodetic observational techniques; these are (1) the interseismic locking depth, (2) the postseismic relaxation time and (3) cumulative postseismic deformation over a given time window. These are key features that numerical models of earthquake cycles along such faults attempt to explain.

1.2.1 Interseismic observations

In between earthquakes, geodetic time series from most mature strike-slip fault settings appear nearly linear in time, at least over available observational timescales (1-2 decades), and the estimated velocities follow an S-shaped function in space (Figure 1), commonly modeled using the functional form $\frac{v^\infty}{\pi} \tan^{-1} \left(\frac{x}{D_{lock}} \right)$ [Savage and Burford, 1973] where v^∞ is the estimated long-term slip

113 rate on the fault and D_{lock} is the depth to which the fault is locked. The estimated locking depth
 114 from this kind of modeling is on the order of 10 – 20 km, which is comparable to the thickness of
 115 the lithosphere over which frictional processes are thought to be dominant [Vernant, 2015]. Deviations
 116 from this expected behavior do appear in the data, such as non-linearities in the time
 117 series and deviations from the \tan^{-1} shape function, however these differences are mostly due to
 118 localized creep episodes (in time and space) or time-invariant creep on some sections of the fault.

119 1.2.2 Postseismic observations

120 Following large earthquakes, time-dependent deformation occurs in the near-field as well as far
 121 away from the fault. This time-dependent signal is typically decomposed into a linear term and
 122 a decaying curvature term (Figure 1). The linear term is assumed to represent background load-
 123 ing due to the motion of tectonic plates, as discussed above. The curvature in the time series is
 124 typically fit with functional forms such as $\sim \log(t)$ and $\sim e^{-t}$, motivated by spring-slider models
 125 of afterslip and creep of a linear viscoelastic material, respectively [Perfettini and Avouac, 2004].
 126 Poroelastic deformation can also contribute to postseismic deformation [Peltzer *et al.*, 1998; Jónsson
 127 *et al.*, 2003], however we ignore this process as we are limited to a two-dimensional anti-plane
 128 geometry where no volumetric strains occur.

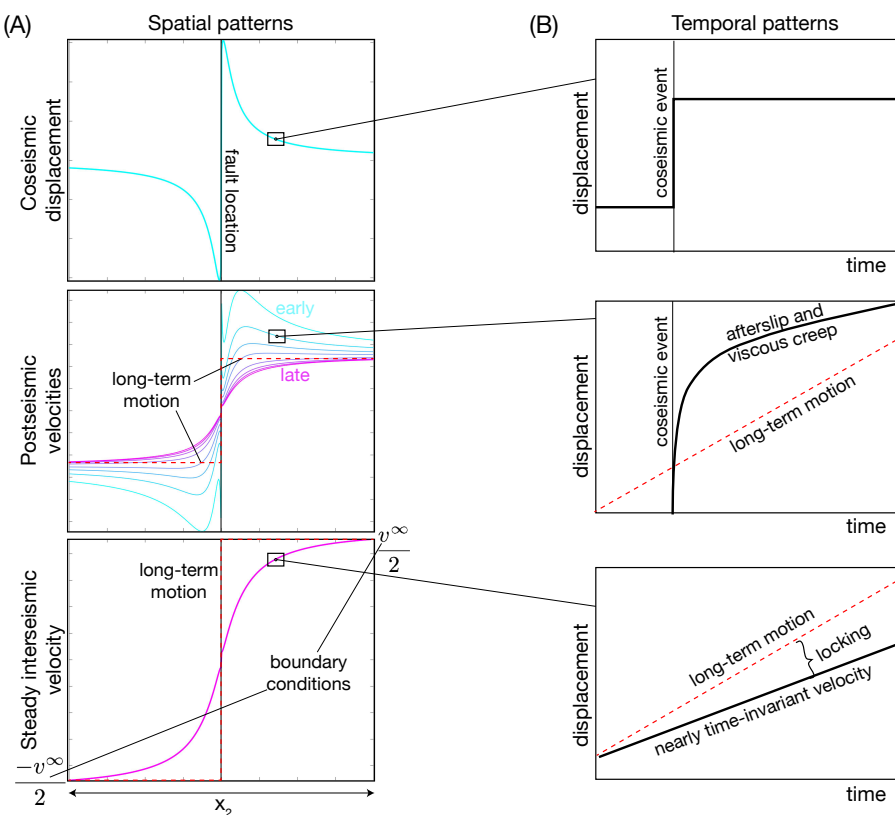


Figure 1: Schematic displacement and velocity evolution recorded at the Earth's surface over the entire earthquake cycle. We show both, (A) the spatial pattern (in colours varying from blue - early postseismic, to pink - late postseismic) and (B) the temporal evolution at a chosen location (black lines). The geodetic predictions from steady rigid block motion is shown in red dashed lines, and deviations from this motion arise due to effects of the earthquake cycle.

129 **1.3 The underlying physical and computational problem**

130 The goal is to infer the rheology of the fault and surrounding medium from the spatio-temporal
131 pattern of surface deformation that contain the features described in the previous section. Two
132 predominant modeling strategies are used for such studies - kinematic modeling of the deforma-
133 tion field and parameter estimation using dynamic models.

134 **1.3.1 Kinematic models**

135 Kinematic models use principles of linear elasticity to develop an impulse-response type rela-
136 tionship between unit inelastic shear and displacements at the Earth's surface [e.g., Segall, 2010;
137 Barbot, 2018]. This set of linear relationships is then used to construct a set of normal equations to
138 estimate slip or strain distributions within the discretized domain to explain the data. The results
139 of such an exercise are estimates of the inelastic source deformation (fault slip - $\Delta s(t)$ and dis-
140 tributed strain - $\Delta \varepsilon(t)$), which then may be combined with elastic stress computations to estimate
141 the relationship between stress change and incremental slip/strain and other derived quantities.

142 **1.3.2 Dynamic models**

143 Dynamic models typically perform physics-based simulations to solve for the stress (σ) and
144 strain-rate evolution ($\dot{\varepsilon}$) within the Earth's lithosphere consistent with quasistatic equilibrium:
145 $\nabla \cdot \sigma(\dot{\varepsilon}) + f_b = 0$. f_b is the equivalent body force applied to the system, which could arise from
146 gravity or imposed slip and tractions as a boundary condition [e.g., Segall, 2010]. To obtain a
147 unique solution for each simulation, boundary conditions and initial conditions need to be spec-
148 ified. Most simulations apply mixed boundary conditions along the edge of the domain (e.g.,
149 Figure 2A). However, the choice of initial conditions remains a difficult task. Many studies treat
150 the pre-earthquake strain rate as a free parameter that is also estimated as part of the inverse prob-
151 lem. The end goal is to determine the coefficients relating σ and $\dot{\varepsilon}$; to do that, an optimization is
152 performed such that the misfit between predicted deformation and the observed deformation
153 time series at sites on the Earth's surface is minimized.

154 **1.3.3 Decomposing the time series**

155 To simplify the inverse problem, many kinematic and dynamic modeling studies decompose the
156 observed tectonic deformation time series into additive contributions arising from (1) a constant
157 in time but spatially variable velocity field and (2) residual terms that are supposed to correspond
158 to time-dependent postseismic deformation (Figure 1). This simplification helps split the spatial
159 domain of the problem into a computationally convenient framework - by neglecting the spatially
160 variable velocity field, post-earthquake relaxation studies need only model inelastic deformation
161 sources that satisfy a zero-displacement boundary condition; a condition that is satisfied trivially
162 for a finite deformation source. A point to note is that this linear decomposition of the time series
163 holds exactly for linear dynamical systems, but can be a source of error and bias if the rheology is
164 non-linear.

165 **1.3.4 Viscoelastic earthquake cycle models**

166 To circumvent issues related to far-field boundary and initial conditions, as well as data decom-
167 position, numerical studies can focus on periodic earthquake cycles. These class of models have
168 been developed in an effort to predict and explain time-dependent earthquake cycle deformation

169 consistent with not only a single earthquake, but the cumulative effects of periodic earthquake
170 sequences integrated over time (across 10's or 100's of earthquakes) to reach an approximately
171 cycle invariant state.

172 Analytic and semi-analytic interseismic velocity models have been developed assuming linear
173 viscoelastic rheologies in both the cases of a finite thickness faulted elastic layer over an un-
174 bounded viscoelastic region [Savage and Prescott, 1978; Cohen and Kramer, 1984; Hetland and Hager,
175 2005, 2006], depth-averaged rheology models [Lehner and Li, 1982; Li and Rice, 1987; Spence and Tur-
176 cotte, 1979], as well as a thin viscoelastic channel [Cohen and Kramer, 1984]. These models use linear
177 Maxwell or Burger's rheologies [Hetland and Hager, 2005] to describe the viscoelastic medium
178 and assume that earthquakes rupture the entire elastic layer. More recent studies account for the
179 mechanical coupling between afterslip and viscoelastic deformation. Since these models involve
180 linear rheologies, the effect of velocity boundary conditions is weak, and the inverse exercise sim-
181 plly involves fitting the curvature in the data with an optimum value of the viscosity (or viscosities
182 for a Burger's body) of the system.

183 An alternative approach is to incorporate rheological parameterizations based on laboratory
184 experiments when solving for equilibrium conditions. These laboratory-derived rheological mod-
185 els are typically determined from studies of single crystal or polycrystal assemblages of minerals
186 thought to be the dominant deforming phase in the crust (quartz) and mantle (olivine) [Hirth,
187 2002; Hirth and Kohlstedt, 2003]. These flow laws are then evaluated at values determined from ge-
188 ological estimates of compositional and thermal variations within the lithosphere to derive rock
189 rheologies at the kilometer scale [Lyzenga et al., 1991; Reches et al., 1994; Takeuchi and Fialko, 2012,
190 2013]. Recent numerical studies have incorporated viscoelastic deformation in simulations of
191 earthquake sequences along a strike-slip fault setting, providing a self-consistent framework that
192 can reproduce all aspects of the earthquake cycle, including spontaneous earthquake nucleation,
193 propagation and arrest [Lambert and Barbot, 2016; Allison and Dunham, 2017, 2021].

194 Both classes of numerical simulations pose their own challenges. Linear viscoelastic models
195 are borne out of computational simplicity and are able to fit many aspects of postseismic defor-
196 mation, however they predict late interseismic locking depths that are significantly deeper than
197 the brittle-ductile transition and are limited in their ability to match observations [e.g., Takeuchi
198 and Fialko, 2012]. Numerical simulations that make use of more sophisticated laboratory-derived
199 flow laws are more numerically challenging and computationally expensive [e.g., Lambert and
200 Barbot, 2016]. While they are able to better explain observations over the entire period between
201 earthquakes, their relatively high computational expense poses a challenge for coupling them
202 into an observational data-driven optimization problem, limiting their current utility for explor-
203 ing and identifying effective constitutive relations of the lithosphere. Thus, there is need for a
204 class of simulations that both satisfies the plate motion-derived kinematic boundary conditions
205 and enables efficient exploration of various rheological parameterizations in order to evaluate
206 what constraints may be afforded from surface deformation data on the effective rheology of the
207 lithosphere.

208 1.4 Aim of this study

209 In this article we examine the use of earthquakes and the related cycle of loading and stress release,
210 in an idealized two-dimensional strike-slip fault geometry, to study the rheological properties of
211 the lithosphere. We develop numerical models of periodic earthquake cycles that can handle
212 all popularly employed rheological models, satisfy the applied boundary conditions in the long-
213 term (integrated over many earthquake cycles) as well as mechanical equilibrium throughout the
214 earthquake cycle, and still remain computationally inexpensive.

This article is protected by copyright. All rights reserved.

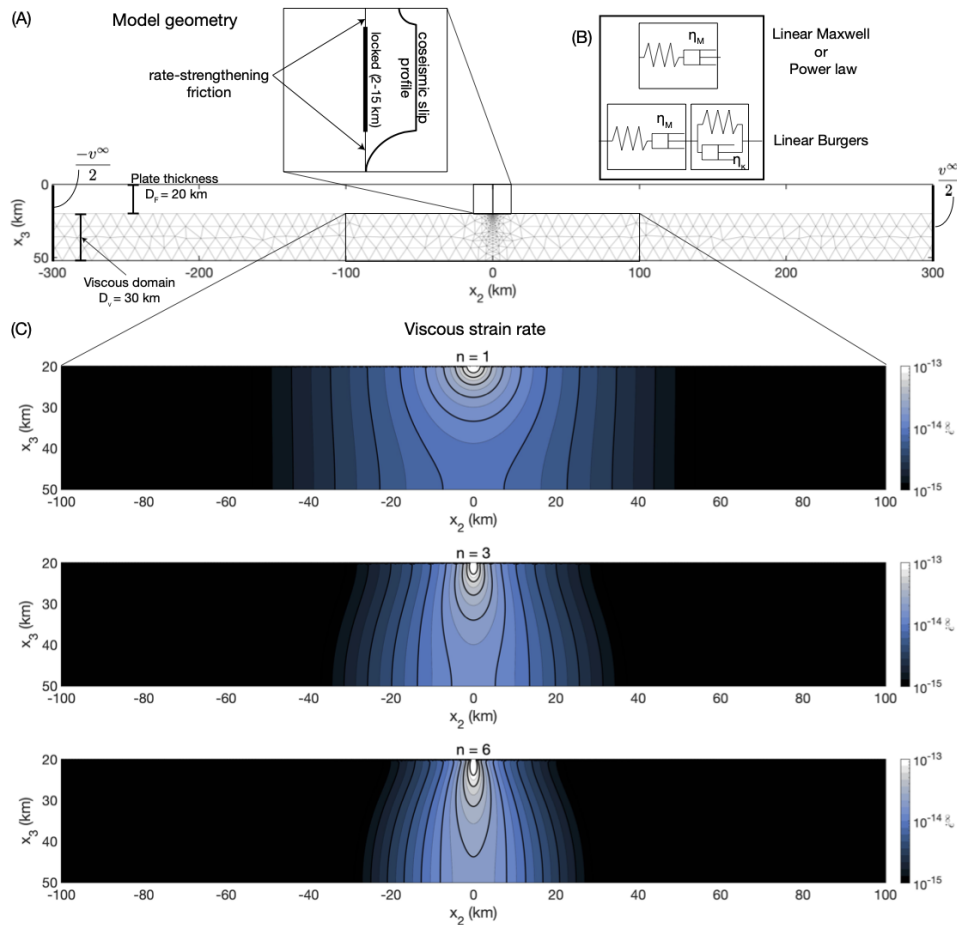


Figure 2: (A) Geometry of the numerical experiments. The domain of the stress calculations are separated into an elasto-frictional domain from 0-20 km depth and a viscoelastic domain from 20-50 km depth. Shear resistance in the frictional domain is given by rate-state friction, while the viscoelastic domain is governed by either a Maxwell rheology (the dashpot can be linear or power-law) or a linear Burgers rheology. (B) These rheologies are shown schematically. η_M - Maxwell viscosity, η_k - Kelvin viscosity. (C) Long-term viscous strain rate $\left(\sqrt{(\dot{\varepsilon}_{12}^\infty)^2 + (\dot{\varepsilon}_{13}^\infty)^2}\right)$ as a function of the power exponent n .

215 We qualitatively compare the predictions from our simulations with observations from strain-
 216 rate regimes that are orders of magnitude apart, i.e., the interseismic period ($\dot{\epsilon} < \dot{\epsilon}^\infty$) and the
 217 postseismic period ($\dot{\epsilon} \geq 10\dot{\epsilon}^\infty$), where $\dot{\epsilon}^\infty$ refers to the steady-state strain rate of the system or the
 218 strain rate averaged over geological timescales (~ 1 Ma). We do not attempt to solve for a best-fit
 219 rheological description like one would in an inverse problem sense. Instead, we show that linear
 220 viscoelastic rheologies need different parameters to explain the interseismic and postseismic pe-
 221 riods of the earthquake cycle, as can be modelled by a Burgers rheology [e.g., Hearn and Thatcher,
 222 2015], while steady state power-law rheologies with power exponent $n \geq 3$ are able to simulta-
 223 neously explain the observed localization of strain preceding great earthquakes on mature faults,
 224 as well as the typical curvature observed in postseismic deformation time series. Discriminating
 225 between Burgers and steady state power-law rheological models using a single earthquake cy-
 226 cle may not be possible using available geodetic time series. However, we discuss how this task
 227 may become significantly more feasible if we include observations over sequences of earthquakes,
 228 particularly of different earthquake size.

2 Methods

230 Our numerical model is developed in an anti-plane geometry i.e., displacements are only in
 231 the out-of-plane x_1 direction, while displacement gradients exist in the $x_2 \times x_3$ plane. We con-
 232 sider a faulted elastic plate supported by a visco-elastic substrate subject to imposed boundary
 233 conditions. The thickness of the elastic plate is D_F , while the viscous substrate extends from
 234 $[D_F, D_F + D_V]$. The elastic plate extends infinitely in the x_2 direction, and the viscous domain is
 235 chosen to be large enough to approximate this infinite x_2 extent (Figure 2A).

236 We first solve the viscous boundary-value problem for the long-term simulation and obtain
 237 the inelastic strain rate and slip rate of the viscous medium and fault respectively. We combine
 238 these long-term rates with an elasticity kernel to formulate a set of Boundary Integral Equations
 239 to simulate the earthquake cycle [Mallick *et al.*, 2021].

2.1 Long-term viscous strain rate

241 The governing equation for the viscous boundary-value problem is posed in terms of the scalar
 242 velocity field $v(x_2, x_3)$,

$$\nabla^2 v(x_2, x_3) = - \left(\frac{\partial \log \eta}{\partial x_2} \frac{\partial v(x_2, x_3)}{\partial x_2} + \frac{\partial \log \eta}{\partial x_3} \frac{\partial v(x_2, x_3)}{\partial x_3} \right) \quad (1)$$

243 where rheology of the substrate is described as follows,

$$\frac{1}{\eta} = A \left(\sqrt{\sigma_{12}^2 + \sigma_{13}^2} \right)^{n-1}; \quad \sigma_{1i} = \eta \dot{\epsilon}_{1i} = \eta \left(\frac{1}{2} \frac{\partial v}{\partial x_i} \right) \quad (2)$$

244 A is a rheological constant, n is the power in the power-law relation $\dot{\epsilon} = A\sigma^n$, η is the viscosity
 245 and the individual stress components are σ_{1i} .

2.1.1 Boundary conditions and solution

247 The boundary conditions on this system are as follows: traction-free at the base ($\sigma_{13}(x_3 = D_F + D_V) = 0$);
 248 lateral edges are subject to anti-symmetric Dirichlet boundaries ($v(x_2 \rightarrow \pm\infty) = \pm \frac{v^\infty}{2}$); the entire
 249 fault slips uniformly at v^∞ resulting in rigid block-like motion of the elastic layer ($0 \leq x_3 \leq D_F$).

This article is protected by copyright. All rights reserved.

250 There exist analytical solutions to this system, at least for spatially uniform values of A, n [Moore
 251 and Parsons, 2015]. The viscous strain rates for a choice of power-law rheology only depend on n
 252 (Figure 2C) and weakly depend on the dimensions of the system. We present these solutions in
 253 terms of rescaled dimensions x'_2, x'_3 , where $x'_3 = \frac{x_3 - D_F}{D_V}$ and $x'_2 = \frac{x_2}{D_V}$. The domain for the solutions
 254 are $0 \leq x'_3 \leq 1, -\omega \leq x'_2 \leq \omega$. We choose the aspect ratio $\omega = 10$, which is sufficiently large such that
 255 there are negligible effects due to the location of the boundary on the strain-rate tensor [Moore and
 256 Parsons, 2015].

$$\begin{aligned}\frac{\dot{\epsilon}_{12}^{\infty}}{v^{\infty}} &= \frac{1}{2\omega} + \frac{1}{\omega} \left(\sum_{m=1}^{\infty} \frac{\cosh \frac{m\pi(1-x'_3)}{\omega\sqrt{n}}}{\cosh \frac{m\pi}{\omega\sqrt{n}}} \cos \frac{m\pi x'_2}{\omega\sqrt{n}} \right) \\ \frac{\dot{\epsilon}_{13}^{\infty}}{v^{\infty}} &= -\frac{1}{\omega\sqrt{n}} \left(\sum_{m=1}^{\infty} \frac{\sinh \frac{m\pi(1-x'_3)}{\omega\sqrt{n}}}{\cosh \frac{m\pi}{\omega\sqrt{n}}} \sin \frac{m\pi x'_2}{\omega\sqrt{n}} \right)\end{aligned}\quad (3)$$

257 We remind the reader that $\dot{\epsilon}$ refers exclusively to the viscous component of the strain rate. The
 258 total strain rate, which is a sum of the viscous and elastic components, is denoted as $\dot{\epsilon}_{\text{total}} =$
 259 $\dot{\epsilon} + \dot{\epsilon}_{\text{elastic}}$.

260 2.2 Periodic earthquake cycle simulations

261 The steady-state solutions for long-term viscous creep rate (Equation 3, Figure 2C) can be used
 262 to compute an equivalent background stressing rate to load earthquake cycle simulations [Mallick
 263 et al., 2021]. We note that without the long-term strain rates, one would have to assign a spatially
 264 variable long-term slip rate and strain rate to drive the earthquake cycle simulations [e.g., Lambert
 265 and Barbot, 2016], but this would not necessarily satisfy the boundary conditions of the system.

266 Using a background stressing rate that is kinematically and dynamically consistent with the
 267 long-term boundary conditions, we transform the time-dependent partial differential equations
 268 for quasi-static equilibrium to a set of coupled ordinary differential equations [e.g., Lambert and
 269 Barbot, 2016; Mallick et al., 2021]. Here we discuss the procedure in brief; we discretize the non-
 270 elastically deforming part of the domain using constant-slip boundary elements for faults and
 271 constant-strain boundary elements for viscous shear. These boundary elements along with Equa-
 272 tion 3 can be used to compute the long-term loading rate of the system as follows,

$$\begin{bmatrix} \dot{\sigma}_F^{\infty} \\ \dot{\sigma}_{12}^{\infty} \\ \dot{\sigma}_{13}^{\infty} \end{bmatrix} = \begin{bmatrix} K_{F,F} & K_{F,12} & K_{F,13} \\ K_{12,F} & K_{12,12} & K_{12,13} \\ K_{13,F} & K_{13,12} & K_{13,13} \end{bmatrix} \begin{bmatrix} -v^{\infty} \\ -\dot{\epsilon}_{12}^{\infty} \\ -\dot{\epsilon}_{13}^{\infty} \end{bmatrix} \quad (4)$$

273 $K_{a,b}$ is a stress-interaction kernel or the boundary-element approximation of the Green's function
 274 tensor that describes the elastic stress transfer to any given element a in response to inelastic shear
 275 (slip on faults and strain in shear zones) on the considered element b [Barbot, 2018].

276 Deviations from the long-term loading rate (Equation 4) drive frictional slip and viscous shear
 277 within the computational domain over the earthquake cycle. The set of coupled ordinary dif-
 278 fferential equations we need to solve is therefore the instantaneous momentum balance for each
 279 boundary element [e.g., Mallick et al., 2021]. To do this, we account for the full elastic interaction
 280 between each point on the fault and in the viscous shear zones using the above described stress

281 interaction kernel.

$$\begin{bmatrix} K_{F,F} & K_{F,12} & K_{F,13} \\ K_{12,F} & K_{12,12} & K_{12,13} \\ K_{13,F} & K_{13,12} & K_{13,13} \end{bmatrix} \begin{bmatrix} v - v^\infty \\ \dot{\varepsilon}_{12} - \dot{\varepsilon}_{12}^\infty \\ \dot{\varepsilon}_{13} - \dot{\varepsilon}_{13}^\infty \end{bmatrix} = \begin{bmatrix} \frac{d\sigma_{\text{friction}}}{dt} \\ \dot{\varepsilon}_{12} \frac{d\eta}{dt} + \eta \frac{d\dot{\varepsilon}_{12}}{dt} \\ \dot{\varepsilon}_{13} \frac{d\eta}{dt} + \eta \frac{d\dot{\varepsilon}_{13}}{dt} \end{bmatrix} \quad (5)$$

282 The left-hand side of this set of equations is the stressing rate in the system arising from elasticity
 283 while the right-hand side is the time derivative of the shear resistance provided by the rheology
 284 of the fault zone and viscoelastic medium. Details about the chosen rheologies are provided in
 285 the following section.

286 2.2.1 Friction and viscous laws

287 Resistive strength evolution on the fault (Equation 5) is described by rate-dependent friction
 288 [Marone *et al.*, 1991] i.e., the resistive strength of the fault is given by $f\sigma_n$ where f is the friction
 289 coefficient and σ_n is the effective normal strength on the fault, and reference values f_0, v_0 .

$$\sigma_{\text{friction}} = f(v)\sigma_n = \left(f_0 + (a - b)\log \frac{v}{v_0} \right) \sigma_n \quad (6)$$

290 The values for each parameter is shown in Table 1, and are only applicable to the regions where
 291 postseismic creep can occur i.e., between 0-2 km and 15-20 km on the fault (Figure 2A).

292 The rheological models we test in the viscoelastic domain are the linear Maxwell, linear Burgers
 293 and power-law rheologies (Figure 2B). The total strain rate in these rheologies are of the form,
 294

$$\dot{\varepsilon}_{\text{total}} = \frac{\dot{\sigma}}{G} + \frac{\sigma}{\eta_M} + \dot{\varepsilon}_k \begin{cases} \frac{\sigma - G\varepsilon_k}{\eta_k}, & \text{Burgers body} \\ 0, & \text{otherwise} \end{cases} \quad (7)$$

295 where $\dot{\varepsilon}_k$ is the Kelvin strain only present for a Burgers body, η_M is the viscosity of the Maxwell
 296 element (for power-law rheologies, η_M in turn is a function of $\dot{\varepsilon}$ i.e., $\frac{d\eta}{dt} \neq 0$ in Equation 5) and G
 297 is the elastic shear modulus of the system.

298 To study the role of viscous rheology in modulating the stress state in this system, and the
 299 associated displacement and velocity field at the free surface, we vary the two parameters used
 300 to describe the rheology in the viscous shear layer for the spring-dashpot bodies (linear Maxwell
 301 and power-law): A, n ; while we vary the Kelvin and Maxwell viscosities for the Burgers material:
 302 η_k, η . We also vary the recurrence time for the earthquake to see how relaxation in the lithosphere
 303 is related to the magnitude of coseismic stress perturbation. We list model parameters we varied
 304 for these simulations in Table 1.

305 2.2.2 Initial conditions from coseismic slip

306 The set of ordinary differential equations we need to solve is Equation 5 in terms of the variables
 307 $[v, \dot{\varepsilon}_{12}, \dot{\varepsilon}_{13}]$, subject to the rheologies in Equation 6-7. To guarantee a unique solution for this system,
 308 we need to determine the initial condition for $[v, \dot{\varepsilon}_{12}, \dot{\varepsilon}_{13}]$. This is done by using the stress change
 309 due to prescribed coseismic slip on the fault to instantaneously change values of $[v, \dot{\varepsilon}_{12}, \dot{\varepsilon}_{13}]$ subject
 310 to their rheological properties.

311 We prescribe coseismic slip as a uniform value of $u^\infty = v^\infty T_{eq}$ within the locked domain ($2 \text{ km} \leq$
 312 $x_{co} \leq 15 \text{ km}$), and tapered in the surrounding section of fault ($0 \text{ km} \leq x_{as} \leq 2 \text{ km} \cup 15 \text{ km} \leq x_{as} \leq$

Table 1: Model parameters for earthquake cycle simulations

Parameter	Range
Fault width	20 km
x_3 scale	30 km
x_2 scale	200 - 500 km
Shear modulus (G)	30 GPa
T_{eq}	50, 100, 200 yrs
v^∞	10^{-9} m/s
Viscous layer (linear Maxwell, power-law)	
Δx	variable mesh size
n	1, 2, 3, 4, 5, 6
A^{-1}	$10^{18}, 3 \times 10^{18}, 7 \times 10^{18}, 10^{19}, 5 \times 10^{19}, 10^{20}$
Viscous layer (linear Burgers)	
Δx	variable mesh size
η_M (Pa-s)	$10^{18}, 5 \times 10^{18}, 10^{19}, 5 \times 10^{19}, 10^{20}$
η_k (Pa-s)	$5 \times 10^{17}, 10^{18}, 5 \times 10^{18}$
Fault parameters	
Δx_3	500 m
$a - b$	0.005
σ_n	50 MPa
f_0, v_0	$0.6, 10^{-6}$ m/s

20 km) such that the stress increase does not exceed 3 MPa and slip within this domain is minimized (Figure 2A). The stress change calculations only require the previously computed Green's function tensor for elastic stress interactions K ,

$$K_{x_{as}, x_{co}} u^\infty(x_{co}) + K_{x_{as}, x_{as}} \Delta u^\infty(x_{as}) \leq 3 \text{ MPa} \quad (8)$$

$$\Delta u^\infty(x_{as}) \sim 0$$

where $u^\infty(x_{co})$ is uniform slip applied within the locked domain and $\Delta u^\infty(x_{as})$ is the tapered slip within the rate-strengthening frictional domain. This is a linear inequality constrained optimization for $\Delta u^\infty(x_{as})$ that is done using the MATLAB function *lsqlin*. The resulting shape of this profile on the fault is shown in Figure 2A.

With the initial conditions determined from coseismic slip, we integrate the system of equations using MATLAB's Runge-Kutta fourth order solver *ode45* to obtain the time history of fault velocity (within the rate-strengthening domain) and viscous strain rates $[v, \dot{\epsilon}_{12}, \dot{\epsilon}_{13}]$ over the entire domain. Since the coseismic slip derived initial conditions only provide a change in the integrable variables, we need to run these earthquake cycles a number of times until we obtain cycle invariant results [e.g., *Hetland and Hager, 2005; Takeuchi and Fialko, 2012*]. In that case, the coseismic slip derived stress change is imposed every T_{eq} years. We find that, depending on rheology, 10-20 cycles is sufficient to obtain cycle invariant results given the rheological parameters and timescales we have chosen.

329 **2.3 Parameters that can be estimated geodetically**

330 The earthquake cycle simulations give us the time history of fault slip rate and viscous strain rates
331 within the viscoelastic medium, which we then combine with displacement Green's functions to
332 predict displacement time series at the free surface [Barbot, 2018]. Since our focus in this article
333 is the behaviour of the viscoelastic domain, we neglect the fault slip rate evolution in the pre-
334 dicted surface deformation time series. We consider two main parameters that can be inferred
335 geodetically that are generally used to describe the period following and leading up to large plate
336 boundary earthquakes. In the postseismic period we estimate the effective relaxation time of the
337 system, t_R ; we describe the interseismic signal using an effective locking depth, D_{lock} .

338 For postseismic relaxation, we consider only the deviation from steady state behaviour i.e.,
339 we remove displacements associated with the long-term motion of the plate boundary or the
340 steady-state strain rates ($\dot{\epsilon}_{12}^\infty, \dot{\epsilon}_{13}^\infty$). We characterize the transient surface displacements during the
341 first 2 years following the earthquake using a two-step procedure. First, we use singular-value
342 decomposition on the displacement time series and extract the temporal component associated
343 with the most dominant singular value. We fit this with the following functional form,

$$u(t) = \beta \left(1 - \exp \left(\frac{-t}{t_R} \right) \right). \quad (9)$$

344 β, t_R are estimated using a MATLAB-based non-linear least squares routine, and t_R gives the best-
345 fit relaxation time of the system over the observational window.

346 Later in the earthquake cycle, we consider the interseismic period as the time period when the
347 maximum surface velocity is smaller than the relative plate velocity, i.e., $|v(x_2)| \leq \frac{v^\infty}{2}$. The resulting
348 velocity field can then be fit to an arc-tangent function [Savage and Burford, 1973],

$$v(x_2) = \frac{v^\infty}{\pi} \tan^{-1} \left(\frac{x_2}{D_{lock}} \right). \quad (10)$$

349 The estimated locking depth controls the effective width of the surface that is experiencing in-
350 terseismic strain, and is thus a physically motivated representation of the spatial pattern of the
351 signal.

352 **3 Results**

353 We describe the surface deformation observations predicted at geodetic sites over the entire earth-
354 quake cycle, as well as the corresponding strain rate evolution within the viscoelastic domain from
355 our numerical experiments (Figure 3, 4). Since we are interested in cycle invariant behaviour, we
356 only present results from the last earthquake cycle; the previous cycles are necessary only for spin
357 up. The results are discussed separately for linear Maxwell, linear Burgers and power-law rhe-
358 ologies in terms of interseismic locking depths (Figure 5), cumulative postseismic displacements
359 (Figure 6) and effective relaxation timescales (Figure 7). We note that our simulations allow for the
360 mechanical coupling between frictional afterslip on the fault and viscous creep in the viscoelastic
361 domain. However, since our focus is on the behaviour of the viscoelastic medium, the surface
362 displacement and velocities that we discuss in subsequent sections do not contain contributions
363 from afterslip.

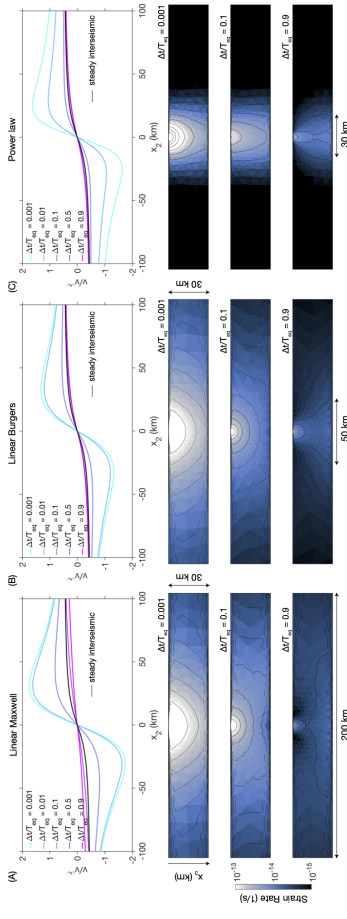


Figure 3: Surface velocity and internal viscous strain rate evolution over the earthquake cycle for different rheologies for a periodic earthquake cycle of $T_{eq} = 50$ years. The rheologies were chosen such that the early postseismic surface velocity field is nearly identical. (A) Linear Maxwell body ($\eta_M = 3 \times 10^{18}$ Pa-s), (B) Linear Burgers body ($\eta_k = 3 \times 10^{18}$ Pa-s), and (C) Power law rheology ($A^{-1} = 3 \times 10^{18}$, $n = 3$). The linear rheologies allow accelerated deformation of significantly larger volume of material compared to the power-law rheology, which promotes localization of strain. This effect is noticeable in all the strain rate snapshots.

364 **3.1 Linear Maxwell**

365 For linear Maxwell rheologies, both the amplitude and effective relaxation timescale of the post-
366 seismic response directly depend on the viscosity (η_M). As η_M increases, the timescale for stress
367 relaxation following the coseismic perturbation (t_R) increases, while the magnitude of the initial
368 jump in strain rate ($\Delta\dot{\epsilon}(\Delta t = 0)$) decreases.

$$t_R = \frac{\eta_M}{G}$$
$$\Delta\dot{\epsilon}_M(\Delta t = 0) = \frac{\Delta\tau_{co}}{\eta_M} \approx \frac{K(v^\infty T_{eq})}{\eta_M} \quad (11)$$

369 A dominant feature from simulations incorporating a linear Maxwell rheology is that they
370 show strain rates that are diffusive in space and in time (Figure 3A). The initial strain rate following
371 the earthquake decays in space as expected from the stress change $\Delta\tau_{co}$. In time, the elevated strain
372 rate is damped as it diffuses outwards. At the end of the earthquake cycle ($\Delta t/T_{eq} \rightarrow 1$), nearly the
373 entire viscoelastic medium is at a uniform strain rate level and the resulting surface velocity field
374 appears to have a near constant spatial gradient (Figure 4D).

375 Many aspects of the evolution of this viscoelastic system can be explained by a single dimensionless variable, $\alpha_M = \frac{T_{eq}}{2t_R} = \frac{GT_{eq}}{2\eta_M}$ [Savage and Prescott, 1978; Savage, 2000]. Models with $\alpha_M \gg 1$, in
376 our simulations this mainly arises from low η_M , generate relatively large magnitude postseismic
377 deformation early in the earthquake cycle (Figure 6) and predict relatively small near fault velocity
378 gradients late in the earthquake cycle (Figure A3, 5D). Conversely, if $\alpha_M \ll 1$ or η_M is large,
379 the system response approaches the elastic limit where there is negligible viscous response and
380 the predicted surface velocities vary only moderately around the steady state elastic expectation
381 throughout the earthquake cycle (Figure A3, 5A-B).

383 **3.2 Linear Burgers**

384 The linear Burgers rheology is characterized by two separate timescales: a short-term anelastic
385 timescale $\frac{\eta_k}{G}$ controlled by the viscosity of the Kelvin element, and a long-term Maxwell timescale
386 $\frac{\eta_M}{G}$ (assuming $\eta_k < \eta_M$) [Müller, 1986; Hetland and Hager, 2005]. Only the creep associated with
387 the Maxwell element is recorded as permanent strain, the anelastic term is significant for geodetic
388 observations but does not leave a record in the long-term.

389 Similar to the linear Maxwell case, the linear Burgers body also exhibits a tendency to diffuse
390 strain rate away from the fault with time (Figure 3C). This pattern depends on three variables
391 - T_{eq} , and the two relaxation times associated with η_k and η_M . Large values of η_k, η_M and small
392 values of T_{eq} , lead to small stress perturbations and hence minimal deviation from a time-invariant
393 steady-state model. Small values of η_k and η_M , or large values of T_{eq} lead to more pronounced
394 earthquake cycle effects.

395 **3.2.1 Interseismic locking depth**

396 Late interseismic locking depths show systematic dependence on only two parameters - η_M and
397 T_{eq} (Figure 5C). This indicates that for the parameter range we explore here, the late interseismic
398 behaviour is effectively controlled by the dimensionless variable, α_M which we discussed in the
399 linear Maxwell case. Thus, small α_M values (large η_M) result in locking depth estimates comparable
400 to purely frictional-elastic simulations (Figure 5D).

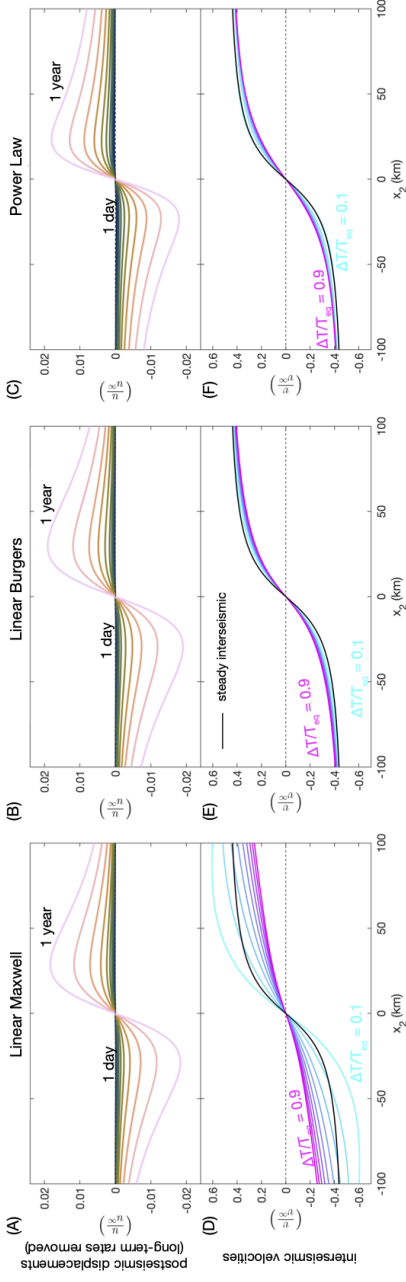


Figure 4: Surface predictions of postseismic displacements and interseismic velocities for different rheologies for a periodic earthquake cycle of $T_{\text{eq}} = 100$ years. The rheologies are chosen such that the cumulative postseismic after 1 year is nearly identical for all three models. (A)-(C) Cumulative postseismic displacements normalized by the coseismic slip amount ($u^\infty = v^\infty T_{\text{eq}}$) for times varying from 1 day to 1 year. (D)-(F) Interseismic velocities compared to the steady interseismic expectation (black line).

401 **3.2.2 Postseismic creep and relaxation time**

402 Linear Burgers bodies do not have a single relaxation timescale, and thus our estimates of t_R
403 depend on the time window that is considered. We consider a 2-year time window, which is a
404 typical observational window used in geodetic studies, in order to estimate the relaxation time
405 and effective viscosity of the system. In most of our simulations, this estimated relaxation time
406 corresponds to sampling the viscous relaxation controlled by η_k (see caption in Figure 6).

407 **3.3 Power-law**

408 Our numerical experiments governed by power-law rheologies are characterized by two main fea-
409 tures - (1) the interseismic locking depths appear to be a constant in time and only weakly sensitive
410 to the parameters we varied (Figure 5A-B), and (2) the postseismic relaxation timescale and am-
411 plitude appear to depend on the coseismic slip amplitude and conform poorly to the $\exp(-t/t_R)$
412 functional form we chose to fit it with (Figure 4C, 7B), i.e., the curvature in the timeseries is closer
413 to a logarithmic decay than the exponential function we chose [e.g., Montési, 2004].

414 **3.3.1 Localized deformation and interseismic locking depth**

415 For our simulations with power-law rheologies, deformation throughout the entirety of the earth-
416 quake cycle is significantly more localized in space than as observed for the linear viscoelastic
417 rheologies discussed above (Figure 3C). The extent of localization depends on the power expo-
418 nent n as well as the rheological parameter A . We contrast this with the fact that the solution to
419 the long-term viscous boundary value problem does not depend on A (Equation 3). Thus, our
420 simulation results suggest that both A and n may be inferred from geodetic data collected over the
421 entire earthquake cycle.

422 Larger stress exponents n favor increased localization while large coefficients A reduce the
423 impact of stress perturbations from coseismic slip, similar to how the magnitude of the viscosity
424 of linear rheologies controls the change in strain rates in Equation 11. While the degree of strain
425 localization depends on the power law stress exponent, for the parameter space explored, we
426 find that models with power law exponents $n \geq 3$ exhibit nearly identical late interseismic locking
427 depths (Figure 5A,D), and are generally comparable to simple back-slip models of interseismically
428 locked faults.

429 **3.3.2 Postseismic creep and relaxation time**

430 The postseismic deformation time series is not expected to conform to the exponential functional
431 form we used to fit the time series. This is because the exponential function is a solution to the
432 linear viscoelastic problem, and the outputs of a power-law rheology correspond to an effective
433 viscosity that systematically increases in time [Montési, 2004]. However, since we consider time
434 windows on the order of 1-2 years, the relaxation timescale can be fit using a linear viscoelastic ap-
435 proximation to estimate an average relaxation time over that window. These relaxation timescales
436 are not only dependent on rheological parameters A, n but are a function of the earthquake size,
437 parameterized here in terms of coseismic slip (Figure 6).

438 For a given set of rheological parameters A, n (for $n > 1$), the cumulative postseismic deforma-
439 tion over a given time window (in this case $\Delta t = 2$ years), even when normalized by the coseismic
440 slip amount, increases with earthquake size (Figure 7A). The normalized postseismic deformation

following small earthquakes in our simulations ($u^\infty \sim 1.5\text{m}$) amounts to about 30% of the normalized postseismic deformation following the largest earthquakes ($u^\infty \sim 12\text{m}$). On the other hand, the estimated relaxation timescale decreases with increasing earthquake size (Figure 7B).

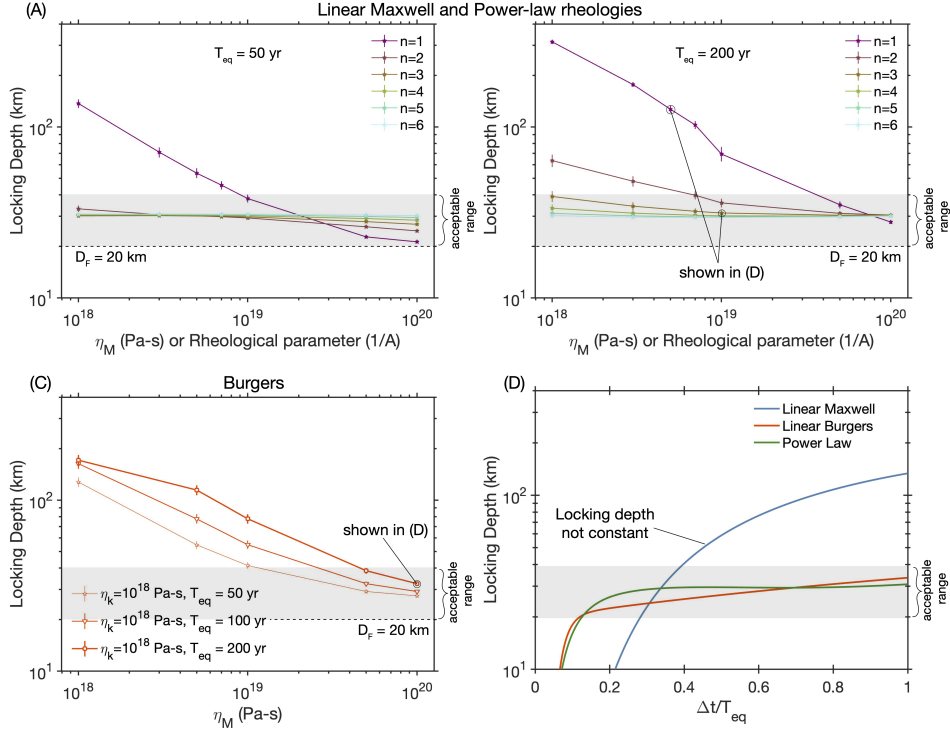


Figure 5: Compilation of late interseismic locking depths for various rheological choices and two different T_{eq} . Locking Depth (assuming an arc-tangent functional fit - $\frac{v^\infty}{\pi} \tan^{-1} \frac{x_2}{D}$) for (A) Linear Maxwell and power-law materials with n varying from 1 to 6 for $T_{eq} = 50$ years. (B) Same as (A) for $T_{eq} = 200$ years. (C) Locking depths for a linear Burgers rheology for a constant η_k and varying η_M and T_{eq} . Late interseismic locking depths show no dependence on η_k . (D) The estimated locking depth varying in time over the interseismic period for different rheologies. Both the power-law body and linear Burgers (with large η_M) show nearly time invariant late-interseismic locking depth.

4 Discussion

We have developed numerical earthquake cycle experiments in order to test how well popular rheological models are able to qualitatively reproduce different observational features in geodetic studies over the entire interseismic period. Our simulation results illustrate the non-uniqueness of rheological models, and their parameters, in explaining postseismic data alone (Figures 5-7).

Our simulations demonstrate that the non-uniqueness in interpreting postseismic data can to some extent be mitigated by incorporating data corresponding to strain accumulation in the late interseismic period (Figure 5). We find that steady-state power-law rheologies with $n \geq 3$ as well as linear Burgers rheology with $\eta_M \approx 10^{20}$ Pa-s and $\eta_k \approx 10^{18}$ Pa-s are able to explain early postseismic relaxation as well as the strain localization observed near strike-slip faults late in the interseismic period. While we do not show it explicitly, nonlinear Burgers rheologies with $n \geq 1$ (with relevant A values) could explain the geodetic data just as well. This is because a steady-state rheology, linear or power-law, is simply a limiting case of an appropriate Burgers rheology

457 where the transient viscosity is much larger than the steady-state value. On the other hand, linear
 458 Maxwell rheologies are simply insufficient to explain the observational features.

459 In the following sections, we first discuss the equivalence between linear Burgers and power-
 460 law descriptions of lithospheric rheology for the earthquake cycle, and then detail geophysical
 461 observations that may be required to convincingly discriminate between these two rheologies.
 462 We then expound on the relationship between inferences of average rheological parameters from
 463 crustal scales and those measured in laboratory experiments, and how a power-law rheology is
 464 consistent with both geodetic observations and laboratory-derived flow laws. Finally, we con-
 465 clude with the implications for stress transfer and the associated assessment of regional hazard
 466 when frictional and viscous creep are mechanically coupled.

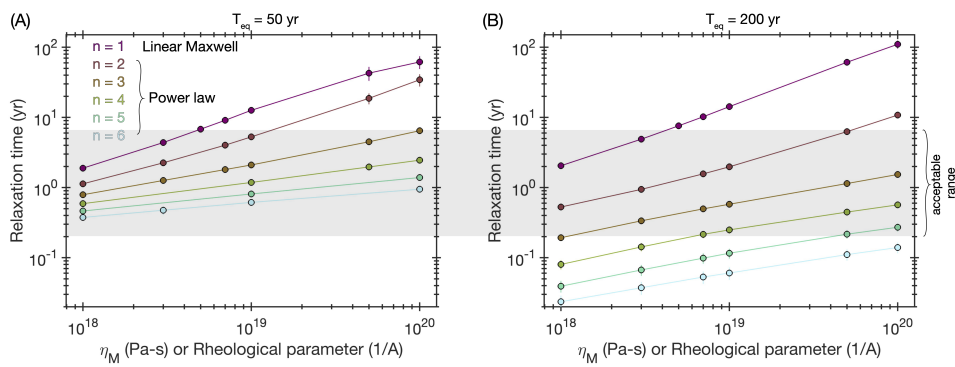


Figure 6: Postseismic relaxation times for linear Maxwell and power law bodies estimated over a 2-year period following the earthquake for a recurrence interval of (A) 50 years and (B) 200 years. Increased T_{eq} leads to larger coseismic slip ($u^\infty = v^\infty T_{eq}$), and hence larger stress change to drive postseismic creep. Linear Maxwell bodies follow a stress-independent relaxation time given by $t_R \approx \frac{\eta_M}{G}$. The relaxation time of power law bodies show a significant reduction for larger coseismic slip. We do not show the results for Burgers bodies, since their relaxation times over the given time window are exactly as predicted by the viscosity of the Kelvin element $t_R \approx \frac{\eta_k}{G}$.

467 4.1 The effective rheology of the lithosphere

468 Geodetic investigations of lithospheric rheology, specifically the lower crust and uppermost man-
 469 ttle, that consider only a relatively short time window ($\Delta t < 5$ years) as is typical of geodetic post-
 470 seismic studies, may not be able to distinguish between any of the rheological models discussed in
 471 this paper (linear Maxwell, linear Burgers and power-law). This is because postseismic geodetic
 472 observations can be reduced to two features - a spatial pattern of cumulative postseismic defor-
 473 mation and the effective relaxation timescale (Figure 7), and there exists a non-unique mapping
 474 between rheological parameters from each of the discussed rheological models to these spatial
 475 and temporal patterns of the deformation data (Figure 7 - 8A-B).

476 However, the three rheological models display diverging behavior as the observational win-
 477 dow gets larger; this is what we exploit during the late interseismic period. Interseismic strain
 478 localization and the stationarity of the locking depth in time is observed in models with either a
 479 power-law rheology or a linear Burgers rheology that approximates the effective viscosity evo-
 480 lution of a power-law body (Figure 8D). In contrast, linear Maxwell rheologies promote diffuse
 481 strain distributions (Figure 3) which manifests as an increase in effective locking depths late in the
 482 earthquake cycle (Figure 5D), a feature that is not seen even in the best monitored strike-slip fault
 483 systems in the world [e.g., Hussain *et al.*, 2018]. This leads us to suggest that Earth's lithosphere

cannot be well-described by a homogenous linear Maxwell body, at least over the timescale of the earthquake cycle.

These findings do not invalidate previous work on estimating the effective viscosity from post-seismic, post-glacial and lake rebound deformation observations assuming a linear Maxwell rheology [e.g., Kenner and Segall, 2003; Johnson and Segall, 2004; Devries and Meade, 2013; Tamisiea *et al.*, 2007; England *et al.*, 2013; Kaufmann and Amelung, 2000; Larsen *et al.*, 2005]. However, the important implication is that these estimates of the average viscosity, or viscosity structure, are tied to the observational window. This detail becomes apparent when comparing the lithospheric viscosities estimated from processes that occur over different timescales; longer observations windows typically show significantly higher viscosities e.g., the viscosity of the upper mantle estimated following deglaciation (since the Last Glacial Maximum), which represents a $\sim 10^4$ year observational time window, is between $10^{20} - 10^{21}$ Pa-s [e.g., Tamisiea *et al.*, 2007; Milne *et al.*, 2001] while typical viscosities estimated in the decade(s) following $M_w > 7$ earthquakes range from $10^{18} - 10^{19}$ Pa-s [e.g., Kenner and Segall, 2003; Pollitz, 2005; Ryder *et al.*, 2007]. Viscosities estimated nearly 50 years after the largest earthquakes in the 20th century appear to favour viscosities in the range $10^{19} - 10^{20}$ Pa-s [Suito and Freymueller, 2009; Melnick *et al.*, 2018; Khazaradze *et al.*, 2002; Freymueller *et al.*, 2000]. Both power-law and linear Burgers rheologies can help reconcile these apparently disparate viscosity estimates, since both processes produce time-dependent viscosities which increase with time since the applied stress perturbation (Figure 8D).

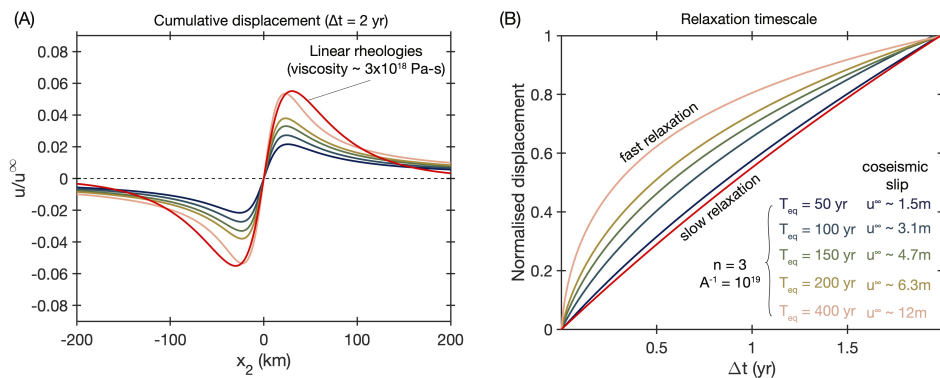


Figure 7: Magnitude dependent postseismic motions for power law bodies. (A) Cumulative post-seismic displacement (steady state component removed) normalized by the coseismic slip amount ($u^\infty = v^\infty T_{eq}$) over 2 years for the same rheology. By increasing the earthquake recurrence interval, we increase the coseismic slip amount. Only power law materials show increasing cumulative deformation with increase in the recurrence interval. (B) As the cumulative deformation increases, the relaxation timescale decreases i.e., the postseismic deformation becomes faster and larger.

502

503 4.1.1 Similarities between power-law and linear Burgers rheologies

504 A question that arises at this point is - how can a linear and power-law rheology satisfactorily
505 explain deformational data throughout the earthquake cycle? The near equivalence between lin-
506 ear Burgers and power-law bodies in our simulations exists because of a non-unique mapping
507 between rheological parameters for each model and the observational features that we use to
508 describe the deformation time series (Figure 8A-C).

509 Consider the viscosity evolution of a power-law body. The power-law rheology results in a
510 lower effective viscosity during the relatively high stress and strain rate postseismic period, and
511 the viscosity gradually increases as stress relaxes and decays to a near time-invariant interseismic

state (Figure 8D). The linear Burgers rheology captures this same kinematic behaviour through completely different dynamics. The Burgers description can be thought of as a technique to describe non-steady state viscous rheology, i.e., there exists a finite timescale or strain over which the system has to evolve to reach the unique mapping between stress and strain rate [Müller, 1986; Hetland and Hager, 2005]. In the case of a linear Burgers rheology, the initial low effective viscosity during the postseismic period is a disequilibrium feature that smoothly evolves to its significantly larger steady state viscosity (Figure 8D).

While the overall kinematics predicted by the two different rheological models appear similar, the predictions from the two models are not identical (Figure 8A inset). Although they would likely be difficult to distinguish after considering the errors and uncertainties in typical geodetic datasets and the various models employed to fit the data [Duputel et al., 2014; Minson et al., 2013].

4.1.2 Magnitude-dependent postseismic motions

Our simulation results suggest that linear Burgers and power-law rheologies may in principle be distinguished by the sensitivity and rate of the postseismic moment release to the magnitude of the coseismic event. For a typical time window ($\Delta t = 2$ yrs), linear viscoelastic rheologies result in postseismic surface deformation that is a linear function of the coseismic slip ($u^\infty = v^\infty T_{\text{eq}}$), and thus can be normalized to produce a constant shape (Figure 7A). Similarly, the temporal evolution of this moment release is invariant of the size of the earthquake (Figure 7B). In contrast, power-law rheologies show a clear magnitude dependence, where the normalized postseismic deformation at the surface is smaller for small events and grows larger with increasing coseismic slip (Figure 7A). The temporal evolution of moment release is also a function of event size with smaller events having much slower relaxation than larger events (Figure 7B).

While this magnitude-dependent behaviour has not been studied thoroughly, there is some evidence to suggest the existence a magnitude-dependent pattern in postseismic observations, supporting the interpretation that lithospheric deformation may follow a power-law rheology. For example, multi-year post-seismic viscoelastic deformation has been clearly observed and documented following $M_w > 7$ continental earthquakes [e.g., Savage and Svart, 2009; Wen et al., 2012; Wang and Fialko, 2018; Freed and Bürgmann, 2004; Freed et al., 2010; Zhao et al., 2021; Pollitz, 2019; Moore et al., 2017; Tang et al., 2019], however observations of notable viscoelastic deformation following slightly smaller ($6.5 < M_w < 7.0$) continental earthquakes are equivocal [e.g. Savage et al., 1998; Wimpenny et al., 2017; Bruhat et al., 2011]. Such distinction in observed postseismic behavior for different sized earthquake ruptures may indicate a critical coseismic stress perturbation required to activate geodetically detectable viscous flow, as would be expected from power-law rheologies (Figure 7). Identifying a clear magnitude-dependence of postseismic viscous response may be challenging given the limited historical data available for individual fault segments, however a careful global compilation of postseismic deformation over a fixed time window following strike-slip fault earthquakes ranging from M_w 6-8 may provide further insight to any systematic magnitude-dependent response, and help discriminate between rheological models of the lithosphere.

4.2 What do estimates of A and n mean at the lithospheric scale?

As previously discussed, geodetic data over a single earthquake cycle is consistent with two classes of rheological models: (1) steady-state flow laws with power law exponents $n \geq 3$ and a range of A values, and (2) an unsteady flow law with $n = 1$, $\eta_k / \eta_M < 0.1$, and $\eta_M \geq 10^{20}$ Pa-s. We note that for unsteady flow laws, we have only explicitly considered the linear Burgers rheology

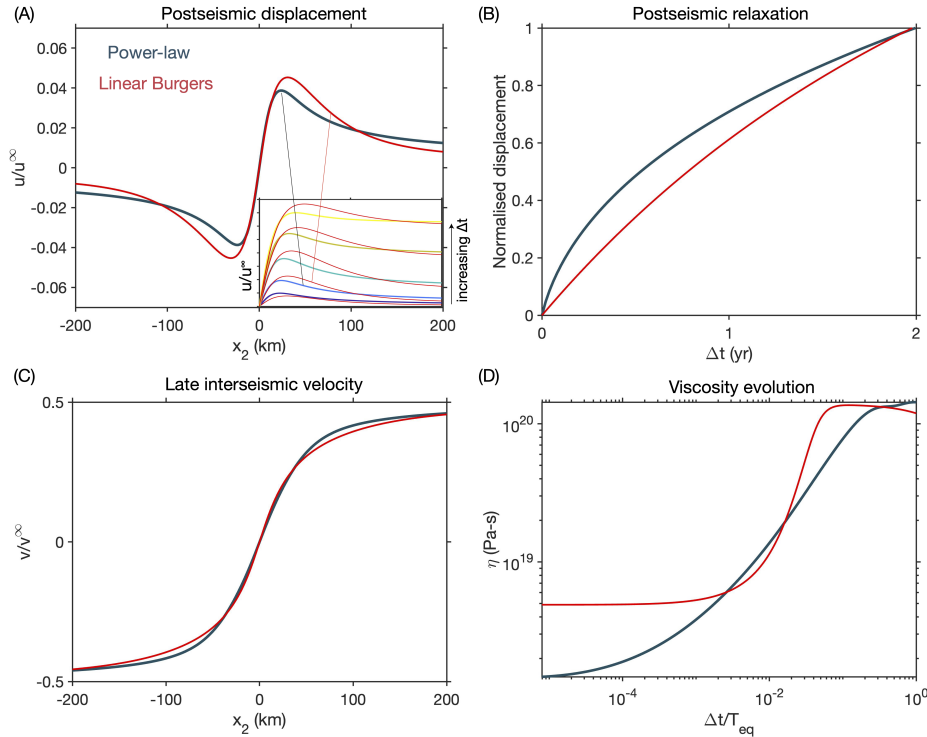


Figure 8: Approximating power-law rheology ($A = 10^{19}, n = 3$) with a linear Burgers body ($\eta_M = 10^{20}$ Pa-s, $\eta_k = 3 \times 10^{18}$ Pa-s) for $T_{eq} = 200$ years. (A) Cumulative displacement for power-law and linear Burgers rheologies after 2 years. The inset shows snapshots of cumulative deformation over increasing time windows of 0.5, 2, 10, 30, 50 years (blue - short timescale, yellow - long timescale). (B) Relaxation time function extracted from the time series. (C) Late interseismic velocity field. (D) Average viscosity evolution in time for both rheological models. $\eta(\Delta t) = \frac{\iint \eta(x_2, x_3, \Delta t) |\dot{\epsilon}(x_2, x_3, \Delta t)| dx_2 dx_3}{\iint |\dot{\epsilon}(x_2, x_3, \Delta t)| dx_2 dx_3}$

where $|\dot{\epsilon}| = \sqrt{\dot{\epsilon}_{12}^2 + \dot{\epsilon}_{13}^2}$

($n = 1$); a power-law rheology with an additional unsteady or transient element can exactly reproduce the observations as well. The principle of parsimony would suggest that a steady-state power-law rheology presents a better representation of the lithosphere, but we turn to the literature from the mineral physics community to expound on the appropriate rheological choice as well as how to interpret what are effectively kilometer-scale averaged estimates of rheological parameters \hat{A} , \hat{n} (and $\hat{\eta}_k$) from geodetic data.

There are two main aspects to this discussion - (1) the contribution of multiple different mechanisms to the inferred parameters $(\hat{A}, \hat{n}, \hat{\eta}_k)$, and (2) the spatially heterogeneous variations of the parameters of various mechanisms to our spatially uniform estimates of the inferred rheological parameters.

4.2.1 Averaging over multiple mechanisms and assemblages

The simplified rheology we employ in this article (Equation 2) is a composite flow law, that under the assumption of linear mixing would attempt to approximate a linear combination of multiple micro-scale processes in the following way,

$$\dot{\varepsilon} = \hat{A}\sigma^{\hat{n}} \approx \sum_i \left[c_i \exp\left(-\frac{Q_i + PV_i^*}{RT}\right) d^{-m_i} C_{\text{fluid}}^{r_i} \right] \sigma^{n_i} \quad (12)$$

This summation indicates simultaneously active processes with different values of the power-law exponent (n_i), each having material specific corresponding activation energy and volumes (Q_i, V_i^*), grain size dependence (m_i) and fluid phase dependence (r_i). c_i is a material and process specific constant, C_{fluid} may refer to either the water fugacity or melt fraction, R is the universal gas constant, T is the absolute temperature of the system and d is a central tendency of the grain size distribution in the sample.

Power-law rheologies for rocks with stress exponents of $n \sim 3 - 4$ are considered representative of dislocation creep, where deformation is accommodated by the migration of dislocations and dislocation planes within the crystal lattice [e.g., *Chopra and Paterson, 1981; Hirth and Kohlstedt, 2003*]; linear rheologies indicate the diffusion of vacancies and defects through the mineral grains and grain boundaries [e.g., *Rutter and Brodie, 2004; Karato et al., 1986*]; intermediate values of n have been suggested to be related to grain boundary sliding [e.g., *Hansen et al., 2011; Goldsby and Kohlstedt, 2001*], although it is important to note that this mechanism is intrinsically coupled to either diffusion or dislocation creep [*Raj and Ashby, 1971; Hansen et al., 2011*]. In addition to mechanical processes, thermal effects can also be relevant to lithospheric deformation. Thermal effects are typically thought of in terms of the steady-state geothermal gradient, but this thermal profile can be perturbed by viscous heating during rapid shear and an associated thermal diffusion [*Takeuchi and Fialko, 2013; Moore and Parsons, 2015*]. As a consequence, the effective power law \hat{n} inferred at the kilometer scale need not be bounded between 1 and 4, but instead may be even higher [e.g., *Kelemen and Hirth, 2007*].

If any of the individual parameters in Equation 12 evolve with incremental strain or time, e.g., temperature or grain size [*Allison and Dunham, 2021; Montési and Hirth, 2003*], then there would not be a unique relationship between $\dot{\varepsilon}$ and σ until a steady state is reached. The viscous creep that would result from this equilibration process is often called 'transient creep', and is an important motivation for invoking Burgers rheology [*Post, 1977; Chopra, 1997; Freed et al., 2012*]. Despite the likely presence of viscous transients, we maintain that the principle of parsimony dictates that we choose steady-state power-law rheologies over Burgers rheologies for modeling geodetic data. To further illustrate this preference, we draw parallels between the aforementioned transient

598 viscous creep and deviations from steady-state frictional strength in rock friction experiments.
599 Unsteady evolution of the friction coefficient is captured by a state variable, θ , which is thought
600 to represent the quality and/or average timescale of asperity contact during frictional sliding
601 [Marone, 1998; Scholz, 1998]. Despite the well-known importance of θ to many aspects of frictional
602 mechanics [Scholz, 2002], geodetic investigations of frictional afterslip are rarely able to resolve
603 the evolution of the frictional state from the data. Even when the state evolution is identified,
604 it is shown to quickly evolve towards steady state within a few hours and may be invisible to
605 typical (sampled daily) postseismic time series [Fukuda *et al.*, 2009; Perfettini and Ampuero, 2008].
606 This argument does not obviate the existence or importance of unsteady strength evolution, but
607 instead emphasizes that it is not necessary to invoke an unsteady Burgers rheology when steady-
608 state power-law rheologies can explain the available geodetic observations. As a result, we are
609 tempted to interpret the value of $\hat{n} \geq 3$ in terms of a rheology dominated by dislocation creep,
610 with possible contributions from thermomechanically-coupled processes such as shear heating
611 and grain boundary sliding.

612 4.2.2 Averaging over spatially variable parameters

613 The inferred \hat{A}, \hat{n} values do not only represent averages over multiple physical and chemical pro-
614 cesses, but also over a spatially varying set of parameters. The dominant contribution of this in
615 Equation 12 likely comes from the depth-dependence of temperature, i.e., $T(x_3) \propto x_3$. However,
616 our ability to geodetically infer spatially varying rheological parameters is limited by the spatial
617 smearing effect of elasticity as well as the apparent homogenization of rheological properties dur-
618 ing shear [e.g., Hetland and Hager, 2006; Almeida *et al.*, 2018; Ray and Viesca, 2019]. This implies that
619 we may at best infer a best-fitting \hat{A}, \hat{n} from a single earthquake cycle, with larger events eliciting
620 a response from greater depths and hence a larger $\hat{A} \propto \exp\left(\frac{-Q}{RT}\right)$. The way forward then is to use
621 sequences of earthquakes (events of different magnitudes and/or depth on the same fault), where
622 each individual earthquake may be mapped to a set of uniform \hat{A}, \hat{n} but these parameters show
623 a consistent pattern, such as a fixed \hat{n} but \hat{A} increases with increasing size or depth of the earth-
624 quake. The implication then is that spatial heterogeneity is necessary to explain the observations
625 and therefore we can infer more about how the lithosphere behaves.

626 4.3 Coupling between frictional slip and viscous creep

627 An important implication of mechanically-coupled models of fault slip and distributed deforma-
628 tion, such as our simulations, is that stress-driven interactions between frictional afterslip on the
629 fault and distributed viscous flow in the lower crust and mantle are not independent processes,
630 as is typically considered in many inverse postseismic modeling studies. This simplification ex-
631 plicitly decouples the mechanical interactions between frictional afterslip and viscous creep, and
632 has been shown to systematically bias the location and amplitude of inferred slip and strain [e.g.,
633 Muto *et al.*, 2019; Peña *et al.*, 2020]. Our simulation results suggest that a permissible simplifica-
634 tion may be to treat earthquake-driven viscoelastic relaxation as an independent process, while
635 afterslip is driven by the coseismic stress change as well as the subsequent viscous flow of the
636 bulk medium (Figure A2). We highlight this by noting the amplitude and temporal evolution of
637 afterslip is markedly different between simulations that consider a purely elastic medium versus
638 a viscoelastic medium (Figure 9).

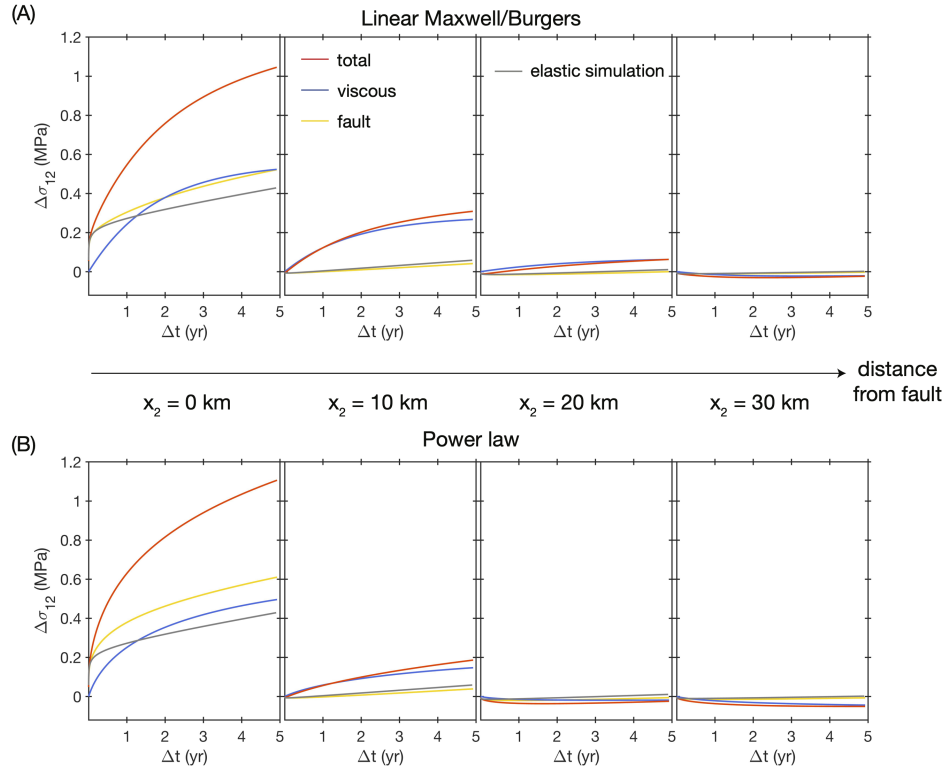


Figure 9: Stress change and decomposition into contributions from fault slip and viscous shear for (A) linear Burgers rheology ($\eta_k = 3 \times 10^{18}$, $\eta_M = 10^{20}$ Pa-s) with effective viscosity $\sim 5 \times 10^{18}$ Pa-s in the plotted time window, and (B) power law rheology with $n = 3, A^{-1} = 10^{19}$. Stress is plotted at 0, 10, 20 and 30 km away from the fault at 10 km depth. Total stress evolution from a nearly elastic model (linear Maxwell simulation with $\eta_M = 10^{20}$ Pa-s) is also shown (gray). The stress evolution over the first 5 years is dominated by the viscoelastic response for linear and power-law rheologies. Additionally, due to the mechanical coupling between fault slip and viscous shear, stress transfer from fault slip evolution in the viscoelastic simulations is significantly different from the elastic simulations.

639 **4.3.1 Time-dependent loading rate**

640 The effect of viscoelastic relaxation on afterslip can be thought of as a modification of the stress
641 loading rate along the fault. For an isolated system, the governing equation for frictional slip
642 in response to a coseismic stress step is $k(v^\infty - v(t)) \propto \frac{df(v(t))}{dt}$ where f is the velocity dependent
643 friction coefficient, k is the elastic stiffness and v^∞ is the long-term slip rate of the fault [Marone
644 et al., 1991]. When viscoelastic relaxation of the medium is factored in, the loading term now
645 contains two contributions - a time-invariant contribution from v^∞ , and time-dependent stress
646 transfer due to viscous creep in the surrounding medium [Pollitz, 2017, 2012]. Viscous creep is
647 itself a decaying function in time, with the exact decay rate being a function of the rheology (Figure
648 3). Thus, the effective loading rate for afterslip is no longer time-invariant (Figure A2B) and the
649 resulting time series for slip and stress transferred to the surrounding medium can notably differ
650 from simulations that decouple afterslip and viscous creep (Figure 9).

651 **4.3.2 Regional stress interactions**

652 The difference in time-dependent loading between purely elastic fault models and those consid-
653 ering viscoelastic deformation suggests that viscoelastic interactions are an important ingredient
654 for efforts aimed at modeling regional tectonics and multi-fault interactions, particularly given
655 that the spatial footprint of this distributed deformation can be much larger than that of slip on
656 individual faults (Figure 3-4). Viscoelastic stress interactions have been noted to be relevant to
657 along-strike stress transfer and timing of a recent sequence of great earthquakes on the North
658 Anatolian Fault [Devries and Meade, 2016; Devries et al., 2017], and Southern California [e.g., Freed
659 and Lin, 2001]. More generally, time-dependent loading alters the stress state on the fault preced-
660 ing dynamic rupture. This pre-rupture stress state has been noted to control many aspects of the
661 rupture process from earthquake nucleation to rupture arrest, including the likelihood of ruptures
662 propagating over multiple fault segments [e.g., Zheng and Rice, 1998; Noda et al., 2009; Ulrich et al.,
663 2018; Lambert et al., 2021; Lambert and Lapusta, 2021].

664 Time-dependent loading due to viscous creep may be particularly important when consider-
665 ing interactions between major plate boundary faults and neighboring lower slip rate faults [Freed,
666 2005; Kenner and Simons, 2005]. For low slip rate faults, the loading due to the long-term tectonic
667 loading rate, which is relatively small for low v^∞ , may be overwhelmed by the static stress trans-
668 fer from a nearby earthquake and the corresponding viscous response of the ductile lower crust
669 and mantle (Figure 9). As a result, seismicity on such low slip rate faults may cluster in time
670 with large earthquakes on the major plate boundary fault and may be indicative of coordinated
671 time-dependent loading, as opposed to an individual long-term loading rate of each fault within
672 this system. Future work is needed to develop more realistic treatments of fault loading in larger-
673 scale simulations of fault networks and models of seismic hazard [e.g., Tullis et al., 2012; Shaw et al.,
674 2018], potentially including physically-motivated approximations of viscoelastic contributions to
675 the effective loading rate of fault populations.,

676 **5 Conclusions**

677 Geodetic recordings of earthquake cycle deformation related to large earthquakes provide geo-
678 scientists with one of the best opportunities to estimate the effective rheology of the lithosphere-
679 asthenosphere system. In this article, we showed that combining geodetic observations with nu-
680 matical simulations of the earthquake cycle translate into better estimates of rheological models

681 and relevant parameters. Below we list a number of important contributions and insight from this
682 study.

- 683 1. We developed a numerical framework to model the earthquake cycle, including interactions
684 between frictional sliding on faults and viscous deformation of the upper mantle, that is
685 computationally inexpensive (can be run on personal computers). This facilitates efficient
686 exploration of various rheological models and parameters.
- 687 2. By incorporating geodetic observations throughout the entire earthquake cycle, the ambi-
688 guity associated with commonly used rheological models is reduced. Specifically, a homo-
689 geneous linear Maxwell viscoelastic medium is simply inconsistent with typical geodetic
690 observations.
- 691 3. The average viscoelastic description of the lithosphere may be that of a power-law spring-
692 dashpot system, although Burgers rheologies may also satisfactorily explain the data but
693 invoke more tunable parameters.
- 694 4. Our preferred parameterization of the viscous element in this spring-dashpot system fol-
695 lows a steady-state flow law of the form $\dot{\epsilon} = A\sigma^n$, and the parameter ranges for the pre-factor
696 $1/A$ range from $10^{18} - 10^{20}$ and the power exponent $n \geq 3$. The power exponent $n \geq 3$ may
697 strongly hint at dislocation creep being a dominant process throughout the earthquake cy-
698 cle. However, we caution direct interpretation of these parameters from single earthquake
699 relaxation studies.
- 700 5. Differentiating between these rheologies requires geodetic observations from earthquake se-
701 quences (events of different magnitudes). The postseismic response of power-law rheologies
702 will show strong magnitude-dependence while the linear Burgers body will not.
- 703 6. An important societal consequence of lithospheric viscoelasticity is to modify the spatial and
704 temporal pattern of stress interactions between faults and the surrounding bulk, compared
705 to purely elastic models. This leads to significantly stronger temporal linkage and long-
706 distance interactions, and hence seismicity, between faults than expected by frictional-elastic
707 models of faults.

708 Acknowledgements

709 This research was supported by a Texaco Postdoctoral Fellowship awarded to R.M and partly
710 funded by the Earth Observatory of Singapore. V.L. is supported by a National Science Foun-
711 dation EAR Postdoctoral Fellowship. The authors thank JGR editor Paul Tregoning, associate
712 editor Mike Poland, Hugo Perfettini and an anonymous reviewer for their review and feed-
713 back on this manuscript. The authors are grateful to Roland Bürgmann and Judith Hubbard
714 for discussions and suggestions for this project. No data was used in this study. All the MAT-
715 LAB code required to recreate the results of this study is available at the Caltech data repository
716 <https://data.caltech.edu/records/20257> (DOI:10.22002/D1.20257).

717 **Appendix**

718 **A Equivalence between afterslip and viscous creep**

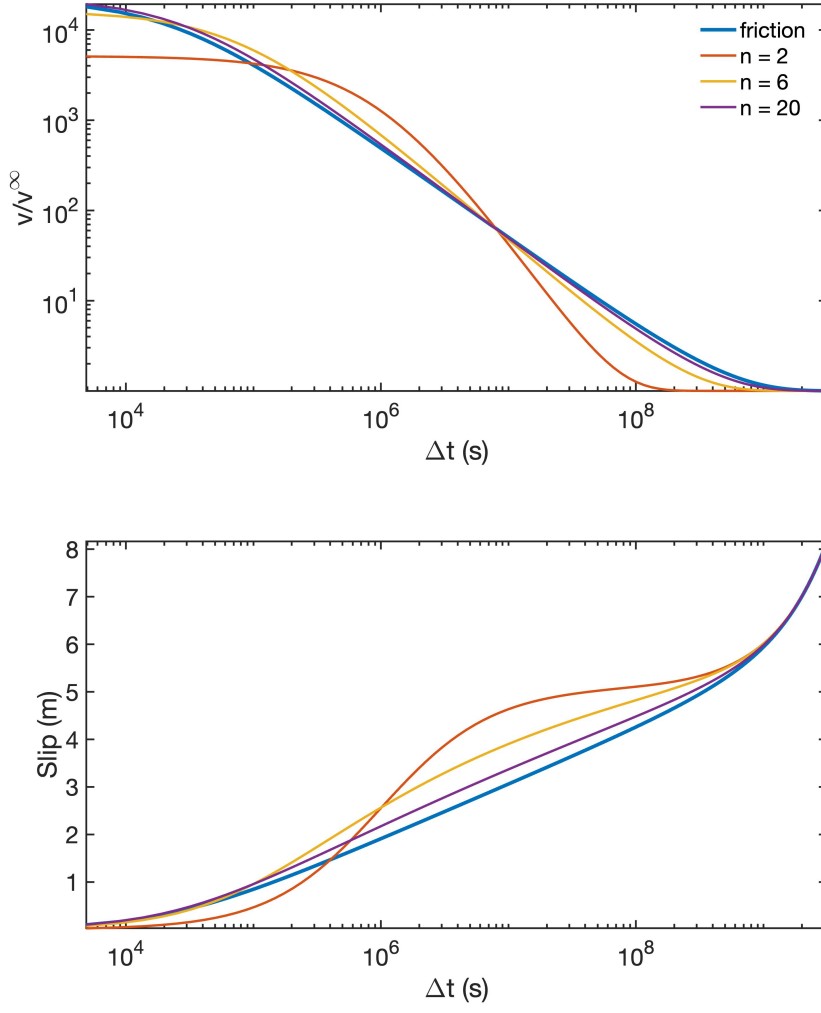


Figure A1: Approximation of frictional slip with a power-law in a simplified spring-dashpot analysis. As power-law exponent n increases, the error in the approximation reduces. The top panel shows velocity evolution for 3 different values of n while the bottom panel shows slip evolution.

719 To demonstrate the equivalence between rate-strengthening frictional sliding and a power-law
720 viscous creep, we consider a common strain rate variable \dot{v} . The governing ODE for a steady-state
721 elasto-frictional system is given by,

$$k(v - v^\infty) = (a - b)\sigma_n \frac{\dot{v}}{v} \quad (13)$$

722 while for a power-law viscoelastic system, the governing ODE is

$$k(v - v^\infty) = \frac{1}{n} \left(\frac{v}{A} \right)^{\frac{1}{n}} \frac{\dot{v}}{v}. \quad (14)$$

This article is protected by copyright. All rights reserved.

723 It is clear that the equivalence between the two systems occurs as $(\frac{v}{A})^{\frac{1}{n}}$ (this is actually the
 724 stress level in the system) approaches a constant value over the domain of v , at least in comparison
 725 to $k(v - v^\infty)$. When $n = 6$, the viscous strain rate changes by ~ 3 orders of magnitude in some of
 726 our simulations. The resulting $(\frac{v}{A})^{\frac{1}{n}}$ varies by ~ 3 over the duration of the entire earthquake cycle.
 727 The variation by a factor of 3 also occurs slowly in time which means that for typical geodetic
 728 observational windows, $n = 6$ is sufficiently close to an equivalent logarithmic system and vice-
 729 versa (Figure A1).

730 **B Relative contributions of afterslip and viscous creep in a cou- 731 pled system**

732 In an elasto-visco-frictional system that explicitly demarcates the non-elastic domain into frictional
 733 and viscous regimes as shown in Figure A2A, we show that the mechanical coupling be-
 734 tween afterslip and viscous creep may be reduced to a one-way coupling problem such that af-
 735 terslip is driven by a time-invariant background loading as well as time-dependent stress transfer
 736 from the viscous domain; the viscous strain rates on the other hand appear to evolve nearly inde-
 737 pendently of afterslip (Figure A2B).

738 The time evolution of the slip rate on a velocity-strengthening frictional fault is given as a
 739 function of the initial condition $v(0)$ and a relaxation timescale t_R ,

$$v(t) = \frac{v(0)}{\frac{v(0)}{v^\infty} + e^{\frac{-t}{t_R}} \left(1 - \frac{v(0)}{v^\infty}\right)} \quad (15)$$

740 The relaxation timescale here corresponds to a different model than the one discussed in Figure 6.
 741 However, considering the parameters we used in our suite of simulations (Table 1), the equivalent
 742 relaxation timescale for the frictional fault is significantly smaller than the relaxation times for at
 743 least the linear Maxwell systems.

744 This decaying signal appears as a straight line on a logarithmic scale, and then will smoothly
 745 transition to the background loading velocity (Figure A2B - dashed lines). However, in the pres-
 746 ence of viscous deformation in the mantle, frictional slip mimics the time evolution of viscous
 747 creep beyond an initial logarithmic decay (Figure A2B). The resulting displacement timeseries at
 748 the free surface reflects this behaviour, and shows that beyond an initial logarithmic growth of
 749 displacements due to frictional slip, this physical process is entirely masked by the surface contrib-
 750 utions of viscous creep (Figure A2C).

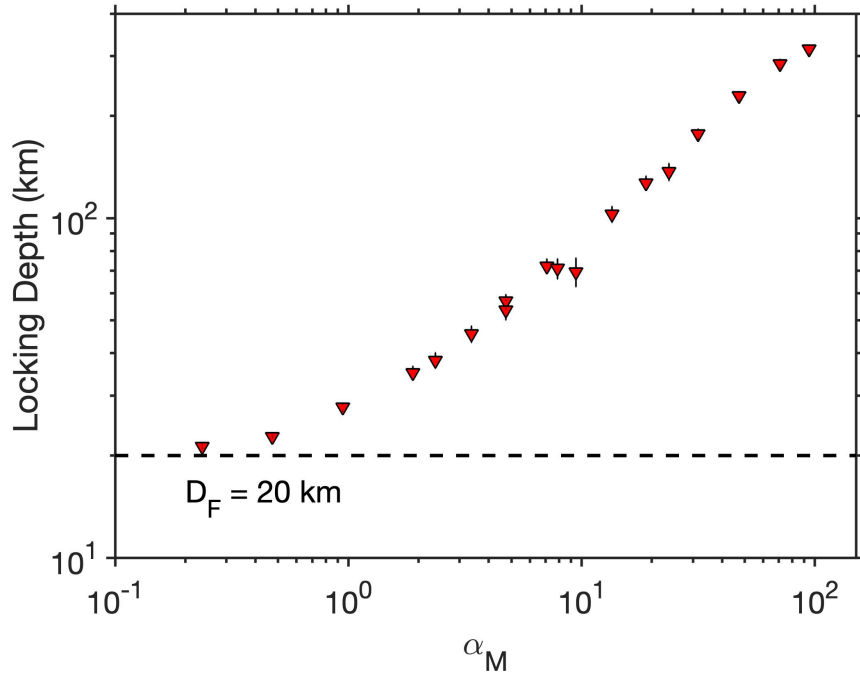


Figure A2: (A) Numerical modeling setup and parameters used for a mechanically coupled visco-elasto-frictional system. (B) Viscous strain rate and on-fault velocity evolution shows the influence of viscous deformation on frictional velocity evolution. Dashed lines show theoretical frictional creep in an isolated elasto-frictional system. (C) Surface displacement time series due to viscous (magenta) and frictional creep (green) arising from lower crustal and upper mantle deformation (shallow creep is not considered here). Left panel shows displacement evolution at $r = 30, 100 \text{ km}$ (continuous line - 30 km, dashed line - 100 km). Right panel shows the percentage contribution of viscous creep to the surface displacement time series as a function of time and space.

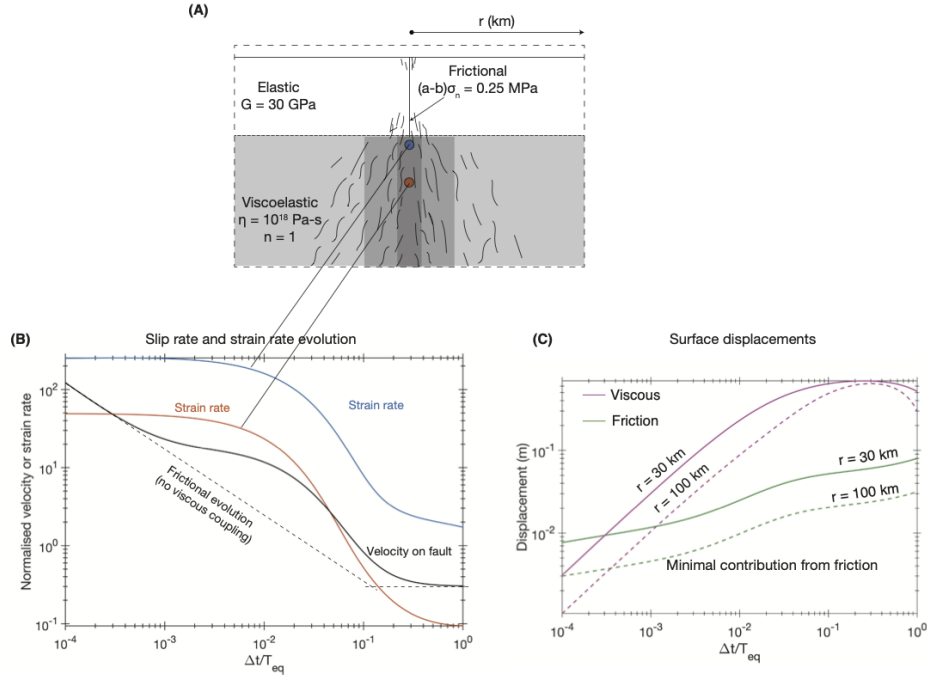


Figure A3: Variation of the geodetically estimated late interseismic locking depth for a linear Maxwell rheology as a function of the rheological parameter α_M . $\alpha_M = \frac{GT_{eq}}{2\eta_M}$ is a dimensionless parameter that combines rheological properties and the recurrence time of the earthquake cycle. Small α_M corresponds to a nearly elastic material, and hence minimal earthquake cycle effects while large α_M corresponds to a low viscosity material and pronounced earthquake cycle effects.

751 **References**

- 752 [1] (2020), *A Vision for NSF Earth Sciences 2020-2030*, National Academies Press, Washington,
753 D.C., doi:10.17226/25761.
- 754 [2] Allison, K. L., and E. M. Dunham (2017), Earthquake cycle simulations with rate-and-state
755 friction and power-law viscoelasticity, *Tectonophysics*, (May), 0–1, doi:10.1016/j.tecto.2017.
756 10.021.
- 757 [3] Allison, K. L., and E. M. Dunham (2021), Influence of Shear Heating and Thermomechanical
758 Coupling on Earthquake Sequences and the Brittle-Ductile Transition, *Journal of Geophysical
759 Research: Solid Earth*, 126(6), 1–28, doi:10.1029/2020jb021394.
- 760 [4] Almeida, R., E. O. Lindsey, K. Bradley, J. Hubbard, R. Mallick, and E. M. Hill (2018), Can the
761 Updip Limit of Frictional Locking on Megathrusts be Detected Geodetically? Quantifying
762 the Effect of Stress Shadows on Near-Trench Coupling, *Geophysical Research Letters*, doi:10.
763 1029/2018GL077785.
- 764 [5] Barbot, S. (2018), Deformation of a Half-Space from Anelastic Strain Confined in a Tetra-
765 hedral Volume, *Bulletin of the Seismological Society of America*, 108(5A), 2687–2712, doi:
766 10.1785/0120180058.
- 767 [6] Bruhat, L., S. Barbot, and J. P. Avouac (2011), Evidence for postseismic deformation of the
768 lower crust following the 2004 Mw6.0 Parkfield earthquake, *Journal of Geophysical Research: Solid
769 Earth*, 116(8), 1–10, doi:10.1029/2010JB008073.
- 770 [7] Bürgmann, R., and G. Dresen (2008), Rheology of the Lower Crust and Upper Mantle: Ev-
771 idence from Rock Mechanics, Geodesy, and Field Observations, *Annual Review of Earth and
772 Planetary Sciences*, 36(1), 531–567, doi:10.1146/annurev.earth.36.031207.124326.
- 773 [8] Chopra, P. N. (1997), High-temperature transient creep in olivine rocks, *Tectonophysics*,
774 93(111).
- 775 [9] Chopra, P. N., and M. S. Paterson (1981), The experimental deformation of dunite, *Tectono-
776 physics*, 78(1-4), 453–473, doi:10.1016/0040-1951(81)90024-X.
- 777 [10] Cohen, S. C., and M. J. Kramer (1984), Crustal deformation, the earthquake cycle, and mod-
778 els of viscoelastic flow in the asthenosphere, *Geophysical Journal International*, 78(3), 735–750,
779 doi:10.1111/j.1365-246X.1984.tb05068.x.
- 780 [11] Devries, P. M., and B. J. Meade (2013), Earthquake cycle deformation in the Tibetan plateau
781 with a weak mid-crustal layer, *Journal of Geophysical Research: Solid Earth*, 118(6), 3101–3111,
782 doi:10.1002/jgrb.50209.
- 783 [12] Devries, P. M., and B. J. Meade (2016), Kinematically consistent models of viscoelastic stress
784 evolution, *Geophysical Research Letters*, 43(9), 4205–4214, doi:10.1002/2016GL068375.
- 785 [13] Devries, P. M., P. G. Krastev, J. F. Dolan, and B. J. Meade (2017), Viscoelastic block models
786 of the North Anatolian fault: A unified earthquake cycle representation of pre- and post-
787 seismic geodetic observations, *Bulletin of the Seismological Society of America*, 107(1), 403–417,
788 doi:10.1785/0120160059.

- 789 [14] Duputel, Z., P. S. Agram, M. Simons, S. E. Minson, and J. L. Beck (2014), Accounting for
790 prediction uncertainty when inferring subsurface fault slip, *Geophysical Journal International*,
791 197(1), 464–482, doi:10.1093/gji/ggt517.
- 792 [15] England, P. C., R. T. Walker, B. Fu, and M. A. Floyd (2013), A bound on the viscosity of
793 the Tibetan crust from the horizontality of palaeolake shorelines, *Earth and Planetary Science
794 Letters*, 375, 44–56, doi:10.1016/j.epsl.2013.05.001.
- 795 [16] Freed, A. M. (2005), Earthquake Triggering By Static, Dynamic, and Postseismic Stress
796 Transfer, *Annual Review of Earth and Planetary Sciences*, 33(1), 335–367, doi:10.1146/annurev.
797 earth.33.092203.122505.
- 798 [17] Freed, A. M., and R. Bürgmann (2004), Evidence of power-law flow in the Mojave desert
799 mantle, *Nature*, 430(6999), 548–551, doi:10.1038/nature02784.
- 800 [18] Freed, A. M., and J. Lin (2001), Delayed triggering of the 1999 Hector Mine earthquake by
801 viscoelastic stress transfer, *Nature*, 411(6834), 180–183, doi:10.1038/35075548.
- 802 [19] Freed, A. M., T. Herring, and R. Bürgmann (2010), Steady-state laboratory flow laws alone
803 fail to explain postseismic observations, *Earth and Planetary Science Letters*, 300(1-2), 1–10,
804 doi:10.1016/j.epsl.2010.10.005.
- 805 [20] Freed, A. M., G. Hirth, and M. D. Behn (2012), Using short-term postseismic displacements
806 to infer the ambient deformation conditions of the upper mantle, *Journal of Geophysical Re-
807 search: Solid Earth*, 117(1), 1–15, doi:10.1029/2011JB008562.
- 808 [21] Freymueller, J. T., S. C. Cohen, and H. J. Fletcher (2000), Spatial variations in present-day
809 deformation, Kenai Peninsula, Alaska, and their implications, *Journal of Geophysical Research:
810 Solid Earth*, 105(B4), 8079–8101, doi:10.1029/1999jb900388.
- 811 [22] Fukuda, J., K. M. Johnson, K. M. Larson, and S. Miyazaki (2009), Fault friction parameters
812 inferred from the early stages of afterslip following the 2003 Tokachi-oki earthquake, *Journal
813 of Geophysical Research*, 114(B4), B04,412, doi:10.1029/2008JB006166.
- 814 [23] Goldsby, D. L., and D. L. Kohlstedt (2001), Superplastic deformation of ice: Experimental
815 observations, *Journal of Geophysical Research: Solid Earth*, 106(B6), 11,017–11,030, doi:10.1029/
816 2000jb900336.
- 817 [24] Hansen, L. N., M. E. Zimmerman, and D. L. Kohlstedt (2011), Grain boundary sliding in
818 San Carlos olivine: Flow law parameters and crystallographic-preferred orientation, *Journal
819 of Geophysical Research: Solid Earth*, 116(8), 1–16, doi:10.1029/2011JB008220.
- 820 [25] Hearn, E. H., and W. R. Thatcher (2015), Reconciling viscoelastic models of postseismic and
821 interseismic deformation: Effects of viscous shear zones and finite length ruptures, *Journal
822 of Geophysical Research: Solid Earth*, 120(4), 2794–2819, doi:10.1002/2014JB011361.
- 823 [26] Henriet, M., J. P. Avouac, and B. G. Bills (2019), Crustal rheology of southern Tibet con-
824 strained from lake-induced viscoelastic deformation, *Earth and Planetary Science Letters*, 506,
825 308–322, doi:10.1016/j.epsl.2018.11.014.
- 826 [27] Hetland, E. A., and B. H. Hager (2005), Postseismic and interseismic displacements near a
827 strike-slip fault: A two-dimensional theory for general linear viscoelastic rheologies, *Journal
828 of Geophysical Research: Solid Earth*, 110(10), 1–21, doi:10.1029/2005JB003689.

- 829 [28] Hetland, E. A., and B. H. Hager (2006), The effects of rheological layering on post-seismic
830 deformation, *Geophysical Journal International*, 166(1), 277–292, doi:10.1111/j.1365-246X.
831 2006.02974.x.
- 832 [29] Hirth, G. (2002), 4 Laboratory constraints on the rheology of the upper mantle, *Reviews in*
833 *Mineralogy and Geochemistry*, 51, 97–120, doi:10.1515/9781501509285-008.
- 834 [30] Hirth, G., and D. L. Kohlstedt (2003), Rheology of the Upper Mantle and the Mantle Wedge:
835 a View From the Experimentalists, *Geophysical Monograph Series*, 138, 83–106.
- 836 [31] Hussain, E., T. J. Wright, R. J. Walters, D. P. Bekaert, R. Lloyd, and A. Hooper (2018), Con-
837 stant strain accumulation rate between major earthquakes on the North Anatolian Fault,
838 *Nature Communications*, 9(1), 1–9, doi:10.1038/s41467-018-03739-2.
- 839 [32] Johnson, K. M., and P. Segall (2004), Viscoelastic earthquake cycle models with deep stress-
840 driven creep along the San Andreas fault system, *Journal of Geophysical Research B: Solid*
841 *Earth*, 109(10), 1–19, doi:10.1029/2004JB003096.
- 842 [33] Jónsson, S., P. Segall, R. Pedersen, and G. Björnsson (2003), Post-earthquake ground
843 movements correlated to pore-pressure transients, *Nature*, 424(6945), 179–183, doi:10.1038/
844 nature01776.
- 845 [34] Kanamori, H., and E. E. Brodsky (2004), The physics of earthquakes, *Reports on Progress in*
846 *Physics*, 67(8), 1429–1496, doi:10.1088/0034-4885/67/8/R03.
- 847 [35] Karato, S.-I., M. Paterson, and D. Fitzgerald (1986), Rheology of Synthetic Olivine Aggre-
848 gates ' for hot pressing . The Specimens were then sleeve and for temperature is jacket 1)
849 and were hot pressed, *Journal of Geophysical Research*, 91(B8), 8151–8176.
- 850 [36] Kaufmann, G., and F. Amelung (2000), Reservoir-induced deformation and continental rhe-
851 ology in vicinity of Lake Mead, Nevada, *Journal of Geophysical Research: Solid Earth*, 105(B7),
852 16,341–16,358, doi:10.1029/2000JB900079.
- 853 [37] Kelemen, P. B., and G. Hirth (2007), A periodic shear-heating mechanism for intermediate-
854 depth earthquakes in the mantle, *Nature*, 446(7137), 787–790, doi:10.1038/nature05717.
- 855 [38] Kenner, S. J., and P. Segall (2003), Lower crustal structure in northern California: Impli-
856 cations from strain rate variations following the 1906 San Francisco earthquake, *Journal of*
857 *Geophysical Research: Solid Earth*, 108(B1), ETG 5–1–ETG 5–17, doi:10.1029/2001jb000189.
- 858 [39] Kenner, S. J., and M. Simons (2005), Temporal clustering of major earthquakes along indi-
859 vidual faults due to post-seismic reloading, *Geophysical Journal International*, 160(1), 179–194,
860 doi:10.1111/j.1365-246X.2005.02460.x.
- 861 [40] Khazaradze, G., K. Wang, J. Klotz, Y. Hu, and J. He (2002), Prolonged post-seismic defor-
862 mation of the 1960 great Chile earthquake and implications for mantle rheology, *Geophysical*
863 *Research Letters*, 29(22), 7–1–7–4, doi:10.1029/2002gl015986.
- 864 [41] Lambert, V., and S. Barbot (2016), Contribution of viscoelastic flow in earthquake cycles
865 within the lithosphere-asthenosphere system, *Geophysical Research Letters*, 43(19), 10,142–
866 10,154, doi:10.1002/2016GL070345.

- 867 [42] Lambert, V., and N. Lapusta (2021), Resolving simulated sequences of earthquakes and
868 fault interactions: Implications for physics-based seismic hazard assessment, *Journal of*
869 *Geophysical Research: Solid Earth*, 126(10), e2021JB022193, doi:<https://doi.org/10.1029/2021JB022193> e2021JB022193 2021JB022193.
- 871 [43] Lambert, V., N. Lapusta, and D. Faulkner (2021), Scale Dependence of Earthquake Rupture
872 Prestress in Models With Enhanced Weakening: Implications for Event Statistics and
873 Inferences of Fault Stress, *Journal of Geophysical Research: Solid Earth*, 126(10), 1–29, doi:
874 10.1029/2021JB021886.
- 875 [44] Larsen, C. F., R. J. Motyka, J. T. Freymueller, K. A. Echelmeyer, and E. R. Ivins (2005), Rapid
876 viscoelastic uplift in southeast Alaska caused by post-Little Ice Age glacial retreat, *Earth and*
877 *Planetary Science Letters*, 237(3-4), 548–560, doi:[10.1016/j.epsl.2005.06.032](https://doi.org/10.1016/j.epsl.2005.06.032).
- 878 [45] Lehner, F. K., and V. C. Li (1982), Large-scale characteristics of plate boundary deforma-
879 tions related to the post-seismic readjustment of a thin asthenosphere, *Geophysical Journal*
880 *International*, 71(3), 775–792, doi:[10.1111/j.1365-246X.1982.tb02797.x](https://doi.org/10.1111/j.1365-246X.1982.tb02797.x).
- 881 [46] Li, V. C., and J. R. Rice (1987), Crustal deformation in Great California earthquake cycles,
882 *Journal of Geophysical Research*, 92(B11), 11,533 – 11,551, doi:[10.1029/JB092iB11p11533](https://doi.org/10.1029/JB092iB11p11533).
- 883 [47] Lyzenga, G. A., A. Raefsky, and S. G. Mulligan (1991), Models of recurrent strike-slip earth-
884 quake cycles and the state of crustal stress, *Journal of Geophysical Research: Solid Earth*,
885 96(B13), 21,623–21,640, doi:[10.1029/91JB02260](https://doi.org/10.1029/91JB02260).
- 886 [48] Mallick, R., R. Bürgmann, K. Johnson, and J. Hubbard (2021), A Unified Framework for
887 Earthquake Sequences and the Growth of Geological Structure in Fold-Thrust Belts, *Journal*
888 *of Geophysical Research: Solid Earth*, 126(9), 1–26, doi:[10.1029/2021JB022045](https://doi.org/10.1029/2021JB022045).
- 889 [49] Marone, C. (1998), Laboratory-Derived Friction Laws and Their Application To Seismic
890 Faulting, *Annual Review of Earth and Planetary Sciences*, 26(1), 643–696, doi:[10.1146/annurev.earth.26.1.643](https://doi.org/10.1146/annurev.earth.26.1.643).
- 892 [50] Marone, C., C. H. Scholz, and R. Bilham (1991), On the mechanics of earthquake afterslip,
893 *Journal of Geophysical Research*, 96(B5), 8441–8452.
- 894 [51] Melnick, D., S. Li, M. Moreno, M. Cisternas, J. Jara-Muñoz, R. Wesson, A. Nelson, J. C. Báez,
895 and Z. Deng (2018), Back to full interseismic plate locking decades after the giant 1960 Chile
896 earthquake, *Nature Communications*, 9(1), 3527, doi:[10.1038/s41467-018-05989-6](https://doi.org/10.1038/s41467-018-05989-6).
- 897 [52] Milne, G. A., J. L. Davis, J. X. Mitrovica, H. G. Scherneck, J. M. Johansson, M. Vermeer, and
898 H. Koivula (2001), Space-geodetic constraints on glacial isostatic adjustment in fennoscandia,
899 *Science*, 291(5512), 2381–2385, doi:[10.1126/science.1057022](https://doi.org/10.1126/science.1057022).
- 900 [53] Minson, S. E., M. Simons, and J. L. Beck (2013), Bayesian inversion for finite fault earthquake
901 source models I-theory and algorithm, *Geophysical Journal International*, 194(3), 1701–1726,
902 doi:[10.1093/gji/ggt180](https://doi.org/10.1093/gji/ggt180).
- 903 [54] Montési, L. G. (2004), Controls of shear zone rheology and tectonic loading on postseismic
904 creep, *Journal of Geophysical Research: Solid Earth*, 109(10), doi:[10.1029/2003JB002925](https://doi.org/10.1029/2003JB002925).

- 905 [55] Montési, L. G., and G. Hirth (2003), Grain size evolution and the rheology of ductile shear
906 zones: From laboratory experiments to postseismic creep, *Earth and Planetary Science Letters*,
907 211(1-2), 97–110, doi:10.1016/S0012-821X(03)00196-1.
- 908 [56] Moore, J. D., and B. Parsons (2015), Scaling of viscous shear zones with depth-dependent
909 viscosity and power-law stress-strain-rate dependence, *Geophysical Journal International*,
910 202(1), 242–260, doi:10.1093/gji/ggv143.
- 911 [57] Moore, J. D. P., H. Yu, C.-H. Tang, T. Wang, S. Barbot, D. Peng, S. Masuti, J. Dauwels, Y.-J.
912 Hsu, V. Lambert, P. Nanjundiah, S. Wei, E. Lindsey, L. Feng, and B. Shibazaki (2017), Imaging
913 the distribution of transient viscosity after the 2016 M w 7.1 Kumamoto earthquake,
914 *Science*, 356(6334), 163–167, doi:10.1126/science.aal3422.
- 915 [58] Müller, G. (1986), Generalized Maxwell bodies and estimates of mantle viscosity, *Geophys-
916 ical Journal of the Royal Astronomical Society*, 87(3), 1113–1141, doi:10.1111/j.1365-246X.1986.
917 tb01986.x.
- 918 [59] Mulyukova, E., and D. Bercovici (2019), The Generation of Plate Tectonics From Grains to
919 Global Scales: A Brief Review, *Tectonics*, 38(12), 4058–4076, doi:10.1029/2018TC005447.
- 920 [60] Muto, J., J. D. P. Moore, S. Barbot, T. Iinuma, Y. Ohta, and H. Iwamori (2019), Coupled
921 afterslip and transient mantle flow after the 2011 Tohoku earthquake, *Science Advances*, (2),
922 1–9.
- 923 [61] Noda, H., E. M. Dunham, and J. R. Rice (2009), Earthquake ruptures with thermal weak-
924 ening and the operation of major faults at low overall stress levels, *Journal of Geophysical
925 Research: Solid Earth*, 114(7), 1–27, doi:10.1029/2008JB006143.
- 926 [62] Peltzer, G., P. Rosen, F. Rogez, and K. Hudnut (1998), Poroelastic rebound along the Lan-
927 ders 1992 earthquake surface rupture, *Journal of Geophysical Research: Solid Earth*, 103(B12),
928 30,131–30,145, doi:10.1029/98jb02302.
- 929 [63] Peña, C., O. Heidbach, M. Moreno, J. Bedford, M. Ziegler, A. Tassara, and O. Oncken (2020),
930 Impact of power-law rheology on the viscoelastic relaxation pattern and afterslip distribu-
931 tion following the 2010 Mw 8.8 Maule earthquake, *Earth and Planetary Science Letters*, 542,
932 116,292, doi:10.1016/j.epsl.2020.116292.
- 933 [64] Perfettini, H., and J.-P. P. Ampuero (2008), Dynamics of a velocity strengthening fault re-
934 gion: Implications for slow earthquakes and postseismic slip, *Journal of Geophysical Research*,
935 113(B9), B09,411, doi:10.1029/2007JB005398.
- 936 [65] Perfettini, H., and J.-P. Avouac (2004), Stress transfer and strain rate variations during
937 the seismic cycle, *Journal of Geophysical Research: Solid Earth*, 109(B6), 1–8, doi:10.1029/
938 2003JB002917.
- 939 [66] Pollitz, F. F. (2005), Transient rheology of the upper mantle beneath central Alaska inferred
940 from the crustal velocity field following the 2002 Denali earthquake, *Journal of Geophysical
941 Research: Solid Earth*, 110(8), 1–16, doi:10.1029/2005JB003672.
- 942 [67] Pollitz, F. F. (2012), ViscoSim earthquake simulator, *Seismological Research Letters*, 83(6), 979–
943 982, doi:10.1785/0220120050.

- [68] Pollitz, F. F. (2017), A note on adding viscoelasticity to earthquake simulators, *Bulletin of the Seismological Society of America*, 107(1), 468–474, doi:10.1785/0120160192.
- [69] Pollitz, F. F. (2019), Lithosphere and shallow asthenosphere rheology from observations of post-earthquake relaxation, *Physics of the Earth and Planetary Interiors*, 293(November 2018), 106,271, doi:10.1016/j.pepi.2019.106271.
- [70] Post, R. L. (1977), High-temperature creep of Mt. Burnet Dunite, *Tectonophysics*, 42(2-4), 75–110, doi:10.1016/0040-1951(77)90162-7.
- [71] Raj, R., and M. F. Ashby (1971), On grain boundary sliding and diffusional creep, *Metallurgical Transactions*, 2(4), 1113–1127, doi:10.1007/BF02664244.
- [72] Ray, S., and R. C. Viesca (2019), Homogenization of fault frictional properties, *Geophysical Journal International*, 219(2), 1203–1211, doi:10.1093/gji/ggz327.
- [73] Reches, Z., G. Schubert, and C. Anderson (1994), Modeling of periodic great earthquakes on the San Andreas Fault: effects of nonlinear crustal rheology, *Journal of Geophysical Research*, 99(B11), 983–1000, doi:10.1029/94jb00334.
- [74] Rutter, E., and K. Brodie (2004), Experimental grain size-sensitive flow of hot-pressed Brazilian quartz aggregates, *Journal of Structural Geology*, 26(11), 2011–2023, doi:10.1016/j.jsg.2004.04.006.
- [75] Ryder, I., B. Parsons, T. J. Wright, and G. J. Funning (2007), Post-seismic motion following the 1997 Manyi (Tibet) earthquake: InSAR observations and modelling, *Geophysical Journal International*, 169(3), 1009–1027, doi:10.1111/j.1365-246X.2006.03312.x.
- [76] Savage, J., and J. Svare (2009), Postseismic relaxation following the 1992 m7.3 landers and 1999 m7.1 hector mine earthquakes, southern California, *Journal of Geophysical Research: Solid Earth*, 114(B1).
- [77] Savage, J. C. (2000), Viscoelastic-coupling model for the earthquake cycle driven from below, *Journal of Geophysical Research*, 105(B11), 25,525, doi:10.1029/2000JB900276.
- [78] Savage, J. C., and R. O. Burford (1973), Geodetic determination of relative plate motion in central California., *Journal of Geophysical Research*, 78(5), 832–845.
- [79] Savage, J. C., and W. H. Prescott (1978), Asthenosphere readjustment and the earthquake cycle, *Journal of Geophysical Research: Solid Earth*, 83(B7), 3369–3376, doi:10.1029/jb083ib07p03369.
- [80] Savage, J. C., J. L. Svare, W. Prescott, and K. W. Hudnut (1998), Deformation following the 1994 northridge earthquake ($m= 6.7$), southern California, *Geophysical research letters*, 25(14), 2725–2728.
- [81] Scholz, C. H. (1998), Earthquakes and friction laws, *Nature*, 391, 37–42, doi:10.1038/34097.
- [82] Scholz, C. H. (2002), *The Mechanics of Earthquakes and Faulting*, 3.
- [83] Segall, P. (2010), *Earthquake and Volcano Deformation*, 517 pp., Princeton University Press, Princeton, doi:10.1515/9781400833856.

- 981 [84] Shaw, B. E., K. R. Milner, E. H. Field, K. Richards-Dinger, J. J. Gilchrist, J. H. Dieterich,
982 and T. H. Jordan (2018), A physics-based earthquake simulator replicates seismic hazard
983 statistics across California, *Science Advances*, 4(8), 1–10, doi:10.1126/sciadv.aau0688.
- 984 [85] Spence, D. A., and D. L. Turcotte (1979), Viscoelastic Relaxation of Cyclic Displacements on
985 the San Andreas Fault, *Proceedings of the Royal Society of London. A. Mathematical and Physical
986 Sciences*, 365(1720), 121–144.
- 987 [86] Suito, H., and J. T. Freymueller (2009), A viscoelastic and afterslip postseismic deformation
988 model for the 1964 Alaska earthquake, *Journal of Geophysical Research: Solid Earth*, 114(11),
989 1–23, doi:10.1029/2008JB005954.
- 990 [87] Takeuchi, C. S., and Y. Fialko (2012), Dynamic models of interseismic deformation and stress
991 transfer from plate motion to continental transform faults, *Journal of Geophysical Research: Solid Earth*, 117(B5), n/a–n/a, doi:10.1029/2011JB009056.
- 992 [88] Takeuchi, C. S., and Y. Fialko (2013), On the effects of thermally weakened ductile shear
993 zones on postseismic deformation, *Journal of Geophysical Research: Solid Earth*, 118(12), 6295–
994 6310, doi:10.1002/2013JB010215.
- 995 [89] Tamisiea, M. E., J. X. Mitrovica, and J. L. Davis (2007), GRACE Gravity Data Constrain
996 Ancient Ice Geometries and Continental Dynamics over Laurentia, *Science*, 316(5826), 881–
997 883, doi:10.1126/science.1137157.
- 998 [90] Tang, C.-H., Y.-J. Hsu, S. Barbot, J. D. P. Moore, and W.-L. Chang (2019), Lower-crustal
1000 rheology and thermal gradient in the Taiwan orogenic belt illuminated by the 1999 Chi-Chi
1001 earthquake, *Science Advances*, 5(2), eaav3287, doi:10.1126/sciadv.aav3287.
- 1002 [91] Tarantola, A. (2006), Popper, Bayes and the inverse problem, *Nature Physics*, 2(8), 492–494,
1003 doi:10.1038/nphys375.
- 1004 [92] Tullis, T. E., K. Richards-Dinger, M. Barall, J. H. Dieterich, E. H. Field, E. M. Heien,
1005 L. H. Kellogg, F. F. Pollitz, J. B. Rundle, M. K. Sachs, D. L. Turcotte, S. N. Ward, and
1006 M. B. Yikilmaz (2012), A comparison among observations and earthquake simulator re-
1007 sults for the allcal2 California fault model, *Seismological Research Letters*, 83(6), 994–1006,
1008 doi:10.1785/0220120094.
- 1009 [93] Ulrich, T., A.-A. Gabriel, J.-P. Ampuero, and W. Xu (2018), Dynamic viability of the 2016
1010 Mw 7.8 Kaikōura earthquake cascade on weak crustal faults, *Nature Communications*, (2019),
1011 doi:10.31223/OSF.IO/AED4B.
- 1012 [94] Vernant, P. (2015), What can we learn from 20 years of interseismic GPS measurements across
1013 strike-slip faults?, *Tectonophysics*, 644, 22–39, doi:10.1016/j.tecto.2015.01.013.
- 1014 [95] Wang, K., and Y. Fialko (2018), Observations and modeling of coseismic and postseismic de-
1015 formation due to the 2015 mw 7.8 gorkha (nepal) earthquake, *Journal of Geophysical Research:
1016 Solid Earth*, 123(1), 761–779.
- 1017 [96] Wen, Y., Z. Li, C. Xu, I. Ryder, and R. Bürgmann (2012), Postseismic motion after the 2001
1018 mw 7.8 kokoxili earthquake in tibet observed by insar time series, *Journal of geophysical re-
1019 search: solid earth*, 117(B8).

- Accepted Article
- 1020 [97] Wimpenny, S., A. Copley, and T. Ingleby (2017), Fault mechanics and post-seismic deformation at bam, se iran, *Geophysical Journal International*, 209(2), 1018–1035.
- 1021
- 1022 [98] Yamashita, F., E. Fukuyama, K. Mizoguchi, S. Takizawa, S. Xu, and H. Kawakata (2015),
1023 Scale dependence of rock friction at high work rate, *Nature*, 528(7581), 254–257, doi:10.1038/
1024 nature16138.
- 1025 [99] Zhao, D., C. Qu, R. Bürgmann, W. Gong, and X. Shan (2021), Relaxation of Tibetan Lower
1026 Crust and Afterslip Driven by the 2001 Mw7.8 Kokoxili, China, Earthquake Constrained by
1027 a Decade of Geodetic Measurements, *Journal of Geophysical Research: Solid Earth*, 126(4), 1–33,
1028 doi:10.1029/2020JB021314.
- 1029 [100] Zheng, G., and J. R. Rice (1998), Conditions under which velocity-weakening friction al-
1030 lows a self-healing versus a cracklike mode of rupture, *Bulletin of the Seismological Society of
1031 America*, 88(6), 1466–1483.